JOURNAL OF GEOPHYSICAL RESEARCH, VOL. 111, C11019, doi:10.1029/2005JC003374, 2006

Breaking waves over a mild gravel slope: Experimental and numerical analysis

Javier L. Lara,[1] Inigo J. Losada,[1] and Philip L.-F. Liu[2]

Received 3 November 2005; revised 12 May 2006; accepted 23 June 2006; published 28 November 2006.

[1] An experimental and numerical study of the effects of a gravel slope on wave shoaling and breaking is presented herein. In the laboratory experiments, fluid velocities, pressure and water surface elevations were measured. Experiments were conducted for both spilling and plunging breakers and for gravel slopes with different gravel sizes. Since gravel slopes caused additional energy dissipation, wave heights in the shoaling zone as well as at the breaking point were reduced. On the other hand, the mean free surface setup inside the surf zone increased. It was also observed that the gravel slope had a stronger influence on the vertical profile of undertow under spilling breaker than on that under a plunging breaker. Moreover, the undertow became weaker over a gravel slope with a larger gravel size. Outside the surf zone, turbulent velocities near the gravel slope were relatively high because of the bottom roughness and percolation. Inside the surf zone, turbulence generated by wave breaking dominated over the gravel bed generated turbulence. The vertical flow induced by the gravel slope changed the turbulence pattern only at cross sections very close to the shoreline. Numerical simulations of the wave breaking processes over a gravel slope were performed. The numerical model was tested by comparing numerical results with experimental data. The model accurately simulated the mean flow quantities. The magnitude of turbulence and turbulence characteristics were also simulated reasonably well.

Citation: Lara, J. L., I. J. Losada, and P. L.-F. Liu (2006), Breaking waves over a mild gravel slope: Experimental and numerical analysis, *J. Geophys. Res.*, *111*, C11019, doi:10.1029/2005JC003374.

1. Introduction

[2] During the last 2 decades, significant advances have been made in improving our understanding of surf zone hydrodynamics, and in particular, the wave breaking process. Most of the recent research in surf zone hydrodynamics has been focused on breaking wave generated turbulence and its transport and dissipation over an impermeable beach [e.g., *Stive*, 1980; *Stive and Wind*, 1982; *Mizuguchi*, 1986; *Nadaoka et al.*, 1989; *Pedersen et al.*, 1993; *Ting and Kirby*, 1994, 1995, 1996; *Petti and Longo*, 2001; *Longo et al.*, 2002]. These studies are applicable to sandy beaches, since the flow velocity within a sandy beach is at least an order of magnitude smaller than those in the water column [*Turner and Masselink*, 1998]. On the other hand, results from these studies cannot be used to describe waves propagating over gravel beaches, whose permeability and grain size are large enough to affect wave motions. Although several laboratory experimental studies have been carried out to investigate wave propagation over rough and permeable beds [*Cox and Kobayashi*, 2000; *Lara et al.*, 2002], comprehensive data describing the wave breaking process over a gravel slope are still lacking.

[3] The wave breaking process also poses great challenges for numerical simulation. Potential flow assumptions are commonly used to describe wave evolution from deep water up to wave breaking point. These assumptions become invalid once the wave breaking process starts. Efforts have been made to parameterize wave breaking processes so that they can be implemented in either the potential flow theory or depth-integrated wave theories, such as Boussinesq-type equations [see *Kirby*, 2003; *Karambas*, 2003]. At present, because of the complexity of the flows generated by breaking waves, these parameterizations are still either too restrictive or not realistic. To date the breaking on waves on permeable slopes has been mostly simulated using depth-integrated potential flow equations, introducing a parameterization of the wave breaking. A very limited validation, which only considers the accuracy of the free surface displacements, has been reported in the literature.

[4] In the last decade, several computational models for breaking waves, based on Navier-Stokes (NS)-type equations, have emerged. These models are able to calculate flows in complex geometries and provide very refined information on the velocity, pressure and turbulence field. A subset of these models is based on the well-known Reynolds Averaged Navier-Stokes (RANS) equations with a turbulence closure model. *Lemos* [1992], *Lin and Liu*

[1]Coastal & Ocean Research Group, Escuela Técnica Superior de Ingenieros de Caminos, Canales y Puertos, Universidad de Cantabria, Santander, Spain.

[2]School of Civil and Environmental Engineering, Cornell University, Ithaca, New York, USA.

0148-0227/06/2005JC003374$09.00

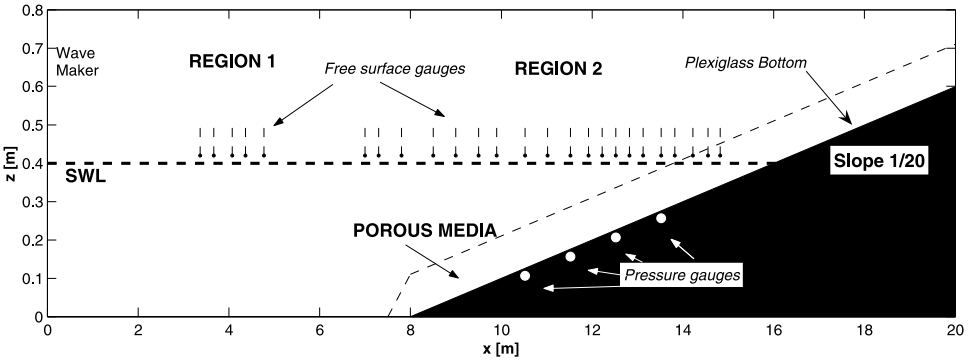

Figure 1. Sketch of the experimental setup and locations of measurement sections.

[1998a, 1998b] and *Bradford* [2000] have employed this approach to study flows in the surf zone. The k-ε turbulence model has been commonly employed in these studies. The free surface location is tracked either by the marker-and-cell (MAC) technique [*Harlow and Welch*, 1965] or by the Volume of Fluid (VOF) method [*Hirt and Nichols*, 1981]. An alternative to the RANS approach is the Large Eddy Simulation (LES). Using different filtering schemes, *Watanabe and Saeki* [1999] and *Christensen and Deigaard* [2001] computed 3D wave breaking over a smooth slope. *Liu et al.* [2005] employed the LES approach to study landslide generated breaking waves and runup. *Losada et al.* [2005] used the 2DV k-ε and 3-D LES modeling to analyze the breaking on low-crested rubble-mound breakwaters. *Watanabe and Saeki* [1999] and *Christensen and Deigaard* [2001] computed 3D wave breaking over a smooth slope. Recently works by *Li et al.* [2005] and *Christensen* [2006] show applications of LES to wave breaking. Since the LES results represent only a single realization of turbulent flows, it is difficult to directly compare LES results with experimental data. Moreover, LES requires analyzing three-dimensional flows and normally demands a fine grid resolution. Thus the suitable computational domain is still quite small.

[5] The RANS models have also been extended for other engineering applications, such as the calculation of wave forces on a composite breakwater or wave transformation over low-crested structures. *van Gent et al.* [1994] proposed a set of governing equations based on the NS equations to describe the unsteady turbulent flows in the porous media. Linear and nonlinear frictional effects were taken into account. Their model (SOLA-VOF [*van Gent*, 1995]) can also simulate non-breaking and breaking wave motions inside and outside permeable structures. However, the model ignores the turbulence generation and dissipation inside the porous media. Other numerical models using the SOLA-VOF method have been presented by *Iwata et al.* [1996] and *Troch and de Rouck* [1998]. *Hsu et al.* [2002] presented a model based on the Volume-Averaged/Reynolds Averaged Navier-Stokes (VARANS) equations, in which the volume-averaged Reynolds stress is modeled by adopting the nonlinear eddy viscosity assumption. The balance equations for the volume-averaged turbulent kinetic energy (TKE) and its dissipation rate are derived by taking the volume-average of the standard k-ε equations. Through the volume-averaging process, the effects of the small-scale turbulence in porous media are introduced. Using the VARANS equations, *Losada et al.* [2003] and *Garcia et al.* [2004] studied wave interactions with low-crested rubble-mound breakwaters for regular waves. Their numerical simulations were validated using measured data of free surface, bottom pressure and fluid velocities from small-scale experiments. Recently *Lara et al.* [2006] have presented a modified version of *Lin and Liu*'s [1998a, 1998b] model including random wave conditions. The efficiency of the modified model in simulating wave interactions with low crested structures was demonstrated for both small- and large-scale experiments.

[6] This paper has two primary objectives. First, we would like to report a set of laboratory data on wave breaking processes and associated flows over a gravel slope. The experimental observations reported here include the water surface elevation, bottom pressure and fluid velocities inside and outside the surf zone. The second objective is to validate the ability of the computational model developed by *Hsu et al.* [2002] and later modified by *Garcia et al.* [2004] and *Lara et al.* [2006] for simulating such complex flows. The beach slope used in the experiments is milder than the typical slope of natural gravel beaches. However, the experimental setup offers the opportunity to investigate both plunging and spilling breakers. It is our aim that once the numerical model is validated by experimental data, the model can then be used to study the natural cobble beaches and revetments in the future.

[7] The paper is organized as follows. In the following section, the experimental setup will be presented first. The experimental procedure and results for regular wave breaking over a gravel slope are discussed in section 3. The envelopes of wave amplitude and mean water level for different gravel sizes are then discussed. The mean flow conditions are also studied to explore the undertow and mean turbulence velocity components. In section 4, the computational model is extensively tested and verified with the experimental data for spilling and plunging wave breakers. Finally, some conclusions are presented in the last section.

2. Experimental Setup

[8] Experiments were conducted in a wave flume at the University of Cantabria, Spain. The wave flume is 24 m long, 0.6 m wide and 0.8 m deep. Waves were generated by a piston-type wavemaker with an active wave absorption

Table 1. Incident Wave Characteristics

Case	h, m	T, s	H_0, m	L_0, m	H_0/L_0	I_{r0}	tan β	Expected Breaking Type
A	0.4	1.2	0.05	1.95	0.0256	0.3122	0.05	spilling
B	0.4	1.2	0.10	1.99	0.0503	0.2230	0.05	spilling
C	0.4	1.2	0.15	2.06	0.0728	0.1853	0.05	spilling
D	0.4	2	0.05	3.72	0.0134	0.4313	0.05	plunging
E	0.4	2	0.10	3.79	0.0264	0.3078	0.05	spilling
F	0.4	2	0.15	3.89	0.0386	0.2546	0.05	spilling
G	0.4	3	0.05	5.83	0.0086	0.5399	0.05	plunging
H	0.4	3	0.10	5.98	0.0167	0.3867	0.05	plunging
I	0.4	3	0.15	6.13	0.0245	0.3196	0.05	plunging
J	0.4	4	0.05	7.94	0.0063	0.6301	0.05	plunging
K	0.4	4	0.10	8.16	0.0123	0.4517	0.05	plunging
L	0.4	4	0.15	8.42	0.0178	0.3746	0.05	plunging

system. At a distance of 8 m from the wavemaker, a plexiglas false bottom was installed to create a slope of 1 on 20. The still water level in the constant-depth region was kept at 0.4 m for all experiments. A sketch of the wave flume is shown in Figure 1.

[9] A gravel layer, being made of wire boxes full of gravels, approximately 11 cm thick, was placed over the Plexiglas slope. Two gravel slopes were constructed with different mean gravel diameters, D_{50} = 19 cm and 39 cm, respectively. The ratios for D_{15}/D_{50} and D_{85}/D_{50} were 0.84 and 1.16, respectively for the larger gravel stones, while they were 0.91 and 1.09, respectively for the smaller gravel stones. The density of the gravel was 2700 kg/m^3 and the porosity was 0.49 for both sizes. For these gravel sizes, the effects of bottom roughness and permeability are significant and at the same time the gravel slope remains immobile throughout the experiments. The free surface elevation was measured by DANTEC resistance gauges at 25 locations. Four differential pressure gauges were fixed on the Plexiglas slope, underneath the gravel layer. The pressure gauges were located at 10.52 m, 11.52 m, 12.52 m and 13.52 m from the wave maker (see Figure 1). Pressure gauges and wave gauges were calibrated twice daily during the experiments. The sampling frequency was 120 Hz.

[10] A two-component LDV with a 5 W Argon ion laser was used to measure the instantaneous velocity. A DANTEC electronic system was employed to split the laser beam into two components, connected to a fiber optic wire. A probe with a focal length of 40 mm was installed at the end of the wire. The probe was located in front of the glass sidewall of the wave flume and a digital transverse system was used to relocate the probe. Finally, video images were also used to identify the location of the breaking point, breaking type and runup.

[11] In the experiments the fifth-order Stokes wave and the Cnoidal wave were generated. Table 1 lists the wave conditions for twelve sets of experiments in terms of wave period, T, and wave height in the constant depth region, H_0. The water depth, h, was kept constant at 0.4 m. These different incident wave conditions resulted in different breaking types and Iribarren numbers, defined as $I_{r0} = \tan\beta/\sqrt{H_0/L_0}$, where tan$\beta$ is the slope of the gravel and L_0 is the wavelength in the constant depth region. The expected breaking type is described in the last column of Table 1.

[12] Experimental data were collected in both the constant depth region and the region over the slope. In the constant depth region, five wave gauges were used to measure the incident waves and to determine the magnitude of reflected waves from the gravel slope. On the slope twenty wave gauges were deployed. Along the centerline of the wave flume instantaneous velocities were measured at 16 vertical cross sections for the gravel slope cases and 25 vertical cross sections for the impermeable slope case, respectively. Along each vertical cross section, velocities were measured at more than 10 elevations below the wave trough level. The exact number of measurement points varies at different cross-sections; the density of measurements is higher near the sloping bottom. The sampling frequency for the velocity measurements was 250 Hz.

3. Experimental Results

[13] In this section, some of the experimental results are reported and discussed. A description of the physical variables and the analysis technique is first introduced. The patterns of the free surface variations, including the amplitude envelopes and the mean water level, are then discussed. Finally, the data for time-mean and turbulent velocity components are presented.

[14] Velocity measurements were separated into the organized flow motions and turbulent fluctuations ($u = \tilde{u} + u'$; $v = \tilde{v} + v'$). The organized flows, ($\tilde{u}$, $\tilde{v}$), include the periodic wave motions, ($\overline{u}, \overline{v}$), and the time-mean current, (U, V). The turbulent velocities, (u', v'), were obtained by filtering the recorded velocities with a band pass filter. The

Table 2. Breaking Location, Breaking Water Depth, Wave Height at the Breaking Point, and Observed Type of Breaking[a]

	Impermeable Bottom				Gravel Bed, D_{50} = 39 mm				Gravel Bed, D_{50} = 19 mm			
Case	x_b, cm	h_b, cm	H_b, cm	Type	x_b, cm	h_b, cm	H_b, cm	Type	x_b, cm	h_b, cm	H_b, cm	Type
A	1465	6.75	6.76	C	...	...	...	NB	...	...	...	NB
B	1350	12.50	11.79	S	1330	13.50	4.39	S	1320	14.00	3.18	S
C	1210	19.50	16.14	S	1300	15.00	7.86	S	1125	23.75	10.88	S
D	1450	7.50	8.06	C	...	...	...	NB	...	...	...	NB
E	1305	14.75	14.11	S	1275	16.25	7.41	S	1210	19.50	10.86	S
F	1210	19.50	18.51	S	1150	22.50	14.18	S	1050	27.50	16.83	S
G	1440	8.00	9.07	P	...	...	...	NB	...	...	...	NB
H	1330	13.50	14.97	P	1260	17.00	10.57	S	1200	20.00	13.79	P
I	1210	19.50	19.96	P	1120	24.00	16.05	P	1070	26.50	17.58	P
J	1460	7.00	6.71	C	...	...	...	NB	...	...	...	NB
K	1360	12.00	11.19	P	1280	16.00	7.38	P	1250	17.50	12.37	S
L	1300	15.00	16.87	P	1250	17.50	12.94	P	1190	20.50	15.15	P

[a]Breaking location, x_b; breaking water depth, h_b; wave height at the breaking point, H_b; C, collapsing; S, spilling; P, plunging; NB, non-breaking wave.

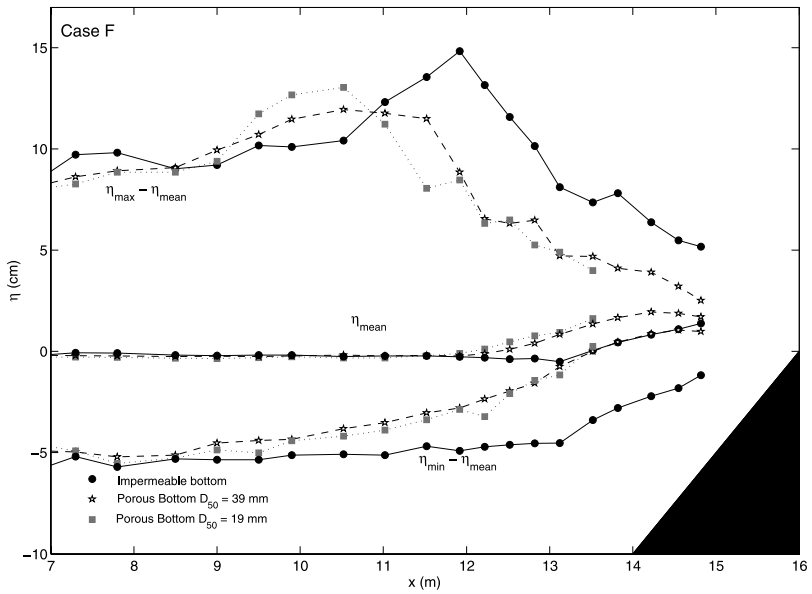

Figure 2. Evolution of the upper and lower envelopes and the mean water level for a spilling breaking case (case F, H = 0.15 m, T = 2 s) for the different slopes.

cut-off frequency for the filter was set at 5 Hz, which was determined by examining the turbulence integral timescale [*Tennekes and Lumley*, 1972]. In the literature different cut-off frequencies have been proposed for different breaking wave conditions. For instance, while *Nadaoka et al.* [1989] used 7 Hz for spilling and plunging breakers, *Ting and Kirby* [1996] employed 5 Hz for the same breaker types. On the other hand, *Sakakiyama and Liu* [2001] selected 5 Hz for both nonbreaking and breaking waves over a porous structure.

[15] The time-mean and turbulent velocities were calculated based on the record of 30 waves. However, additional 20 waves were generated before the actual measurements were taken so as to ensure a quasi steady state condition in the wave tank. Because of the page limitation, only selected experimental results will be presented herein.

3.1. Water Surface Elevations

[16] The spatial variations of water surface elevations are analyzed from shoaling zone to shoreline. Breaking point locations are determined from direct visual observations as well as videotape records of 30 wave breaking events for each experiment. The breaking point of a spilling breaker is defined as the location where air bubbles begin to appear at the wave crest, whereas for a plunging breaker the breaking point is where the front face of the wave becomes nearly vertical [*Bonmarin*, 1989]. The wave characteristics at the breaking point and the type of wave breaking observed for different types of slopes are summarized in Table 2. The water depth at breaker (h_b) denotes the vertical distance measured from the still water surface level to the impermeable Plexiglas slope (see Figure 1), including the gravel layer thickness (11 cm). Under identical incident wave conditions, breaking wave height at the breaking point is smaller for the gravel slope with larger gravels (see case H in Table 2). Clearly, the presence of a gravel slope causes additional energy dissipation before the incident waves reach the breaking point, and thus, reduces the breaking wave height. In some cases, the wave breaking mechanism changes from plunging to spilling (case H) or nonbreaking (case A).

[17] Figures 2 and 3 show the envelopes of free surface fluctuations and the mean water level evolution for a spilling breaker (case F) and a plunging breaker (case I), respectively. In the spilling breaker case (Figure 2), because of the energy dissipation caused by the gravel slope, the wave heights (the vertical distance between upper and lower envelopes) are generally smaller than those over an impermeable slope. As expected, the breaker location for the impermeable slope case is closer to the shore (see Table 2). Similar features of wave envelopes are also observed for the plunging breaker case (Figure 3).

[18] The wave setup inside the surf zone for the gravel slope cases is much higher than that for the impermeable slope case, especially for the plunging breaker, which corresponds to a longer incident wave period. This observation is consistent with a previous study by *Mendez et al.* [2001], which showed that the damping of wave heights along a mild porous slope could result in a setup even without wave breaking. The setup also appears to increase with the gravel size.

3.2. Undertow

[19] Several previous studies have described the undertow profiles under both spilling and plunging breaking waves over an impermeable slope [e.g., *Stive and Wind*, 1982; *Hansen and Svendsen*, 1984; *Ting and Kirby*, 1994]. The undertow is defined as the horizontal component of the time-mean velocity. To completely describe time-mean flow motions over a gravel slope, the vertical component of the time-mean velocity also needs to be analyzed. Useful information such as the effects of percolation induced by the gravel layer can be extracted from vertical velocity analysis.

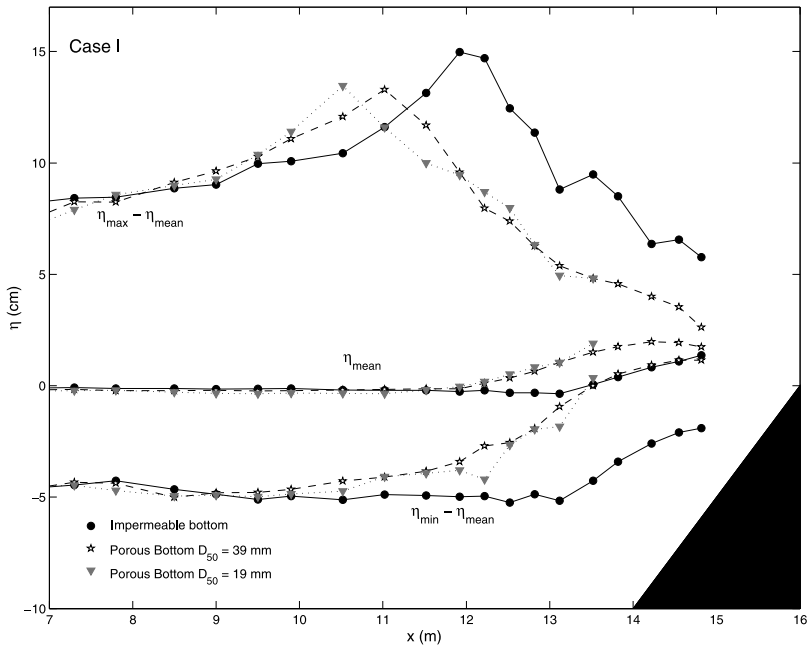

Figure 3. Evolution of the upper and lower envelopes and the mean water level for a plunging breaking case (case I, H = 0.15 m, T = 3 s) for the different slopes.

[20] Thus the profiles of both undertow (U) and time-mean vertical velocity component (V) in the water column are presented in Figures 4 and 5, in which the velocities (U, V) have been normalized by the local wave celerity (c). The local wave celerity was calculated based on the linear wave theory with the water depth (h) (the vertical distance from the still water surface level to the impermeable Plexiglas slope). Consequently, the measured data over three different slopes can be directly compared. In Figures 4 and 5 measurements for three different slopes are plotted in different columns, while data at four different locations are presented in different rows. The first row, row a, corresponds to a location outside the surf zone. Positions inside the surf zone correspond to rows b, c and d. The elevation of the gravel bed is shown as a dotted line (middle and right column). The position of the wave trough is denoted as a dashed line. The position of each section is indicated by the normalized distance to the breaking point $(x - x_b)/h_b$ as well as the dimensionless water depth h/h_b, in which x is the horizontal coordinate, and the subscript "b" denotes the breaking point.

[21] The measurements shown in Figure 4 are for Case F (H = 0.15 m and T = 2 s). Measured undertows over the impermeable bottom (left column) have similar features to those observed in previous studies [e.g., *Hansen and Svendsen*, 1984; *Ting and Kirby*, 1994]. Outside the surf zone, the onshore mass transport induced by the wave motions near the crest is balanced by a return flow (seaward mass transport) below the wave trough level. The undertow velocity appears to decrease linearly with water depth. We note that the undertow observed by *Ting and Kirby* [1994] at the trough level was about $0.05c$, which is almost identical to the value measured in the present case (Figure 4a, plot 1). In the outer surf zone ($(x - x_b)/h_b < 5$, Figure 5b, plot 1), the undertows have become stronger than those outside the surf zone. Once the bore is formed in the inner surf zone ($(x - x_b)/h_b > 5$, plot 1 in Figures 4c and 4d), the vertical profile of the undertow changes; the maximum value is no longer at the wave trough level and appears near the bottom.

[22] In the case of gravel slopes, the undertow profiles outside the surf zone (Figure 4a, plots 2 and 3) do not differ substantially from those over the impermeable slope (Figure 4a, plot 1). For the case of impermeable slope, the maximum values of the normalized undertow are around 0.1 close to the breaking point (Figure 4b, plot 1) and around 0.2 in the inner surf zone. However, over the gravel slopes the maximum undertow values are only around 0.1. This could be the results of less energetic waves over a gravel slope (see wave amplitude in Figure 2).

[23] Outside the surf zone, the time-mean flows are nearly horizontal beneath the wave trough, where the values of the vertical velocity component, V/c, are close to zero for all slopes. However, inside the surf zone, stronger vertical velocities, V/c, are observed. For the permeable slopes, percolation enhanced the vertical velocity. In the outer surf zone, the region influenced by the gravel bed appears to be confined within 50% of the water depth above the gravel. On the other hand, in the inner surf zone, nonzero vertical velocities extend over the entire depth. The undertows are affected more strongly by the large size gravel slope (middle column). The undertow patterns become similar to those over an impermeable slope for the D_{50} = 19 mm bottom (left column), but smaller in magnitude. Vertical velocities are observed to be larger for the slope with larger gravel size because of the strong bottom influence, not only close to the bottom but also in the whole water column in the inner surf zone (Figure 4d, plot 2).

[24] As shown in Figures 4 and 5, for both spilling and plunging cases, the vertical distribution of the undertow is almost identical before wave breaking. The undertows decrease from $U = -0.05c$ below the wave trough to almost

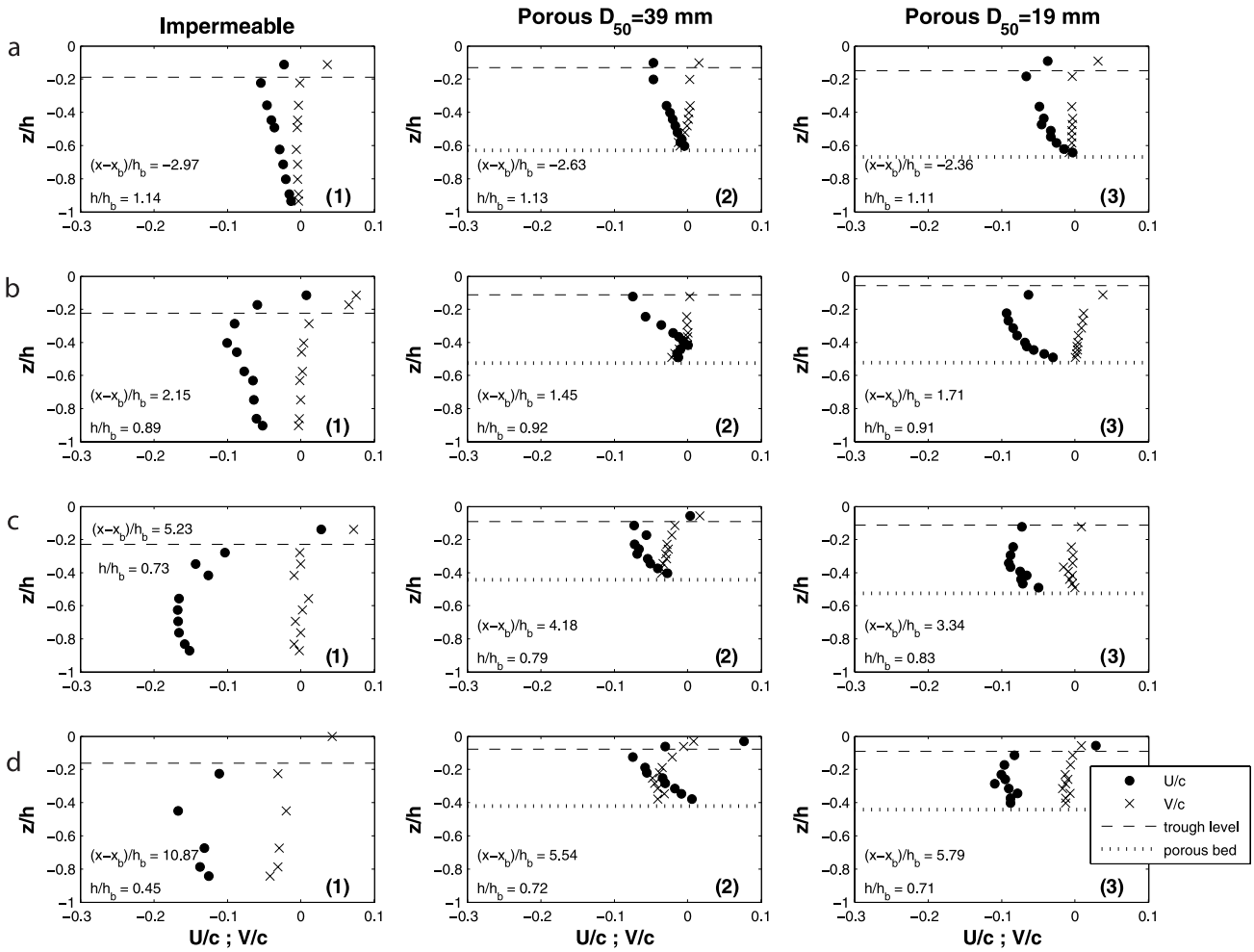

Figure 4. Normalized undertow (dots) and ensemble vertical velocity (crosses) for case F ($H = 0.15$ m, $T = 2$ s). Dashed line, trough level; dotted line, porous layer upper interface.

zero or a small positive value close to the bottom. Again, for the plunging breaker the influence of the gravel slope is confined within a small region above the gravel bed and the influence region is more visible for larger gravel size.

[25] Under the plunging breaker the undertow over the impermeable bottom is uniform vertically inside the surf zone. As *Ting and Kirby* [1994] pointed out, this is the strong mixing of momentum due to plunging wave breaking. Undertow values measured by *Ting and Kirby* [1994] are not of the same order of magnitude as those presented in Figure 5. We note that the experimental setup and wave characteristics are different in these two investigations. The beach slope used by *Ting and Kirby* [1994] is 1/35, while the slope used herein is 1/20. Furthermore, for the plunging breaker case, the Irribaren's number in the present experiment is smaller (0.37 in the present work and 0.60 for Ting and Kirby) yielding differences in the undertow values for plunging.

[26] As shown in Figure 5, in the outer surf zone, the vertical profiles for the undertow (under a plunging breaker) over a gravel slope are no longer uniform in the water column, but decrease with depth (Figure 5b, plots 2 and 3). While a stronger undertow current at the wave trough is observed, the vertical time-mean velocity is almost zero in the entire water column. The influence of the gravel slope is more visible in the inner surf zone. For the larger gravel size slope (plot 2 in Figures 5c and 5d), the undertow profiles are much closer to those for the spilling breaker. Measured undertow values are almost identical to the values presented in Figure 4 for a spilling breaker over the same gravel slope. The normalized vertical time-mean velocity shows negative values and increases within the inner surf zone, suggesting that flows percolate through the gravel slope and lead to a complex three-dimensional flow structure. It is clear that the time-mean velocity inside the gravel slope also plays a significant role in our understanding of the undertow characteristics. Unfortunately, with presently available instrumentations, it is not possible to record the velocities inside the gravel slope.

3.3. Turbulent Velocities

[27] The turbulent velocities presented here are normalized by wave celerity c. Results of the horizontal turbulent velocity (dots) and vertical turbulent velocity (crosses) for a spilling breaker are shown in Figure 6 for case F ($H = 0.15$ m and $T = 2$ s) and in Figure 7 for case L ($H = 0.15$ m and $T = 4$ s), respectively. Data for three different slopes are

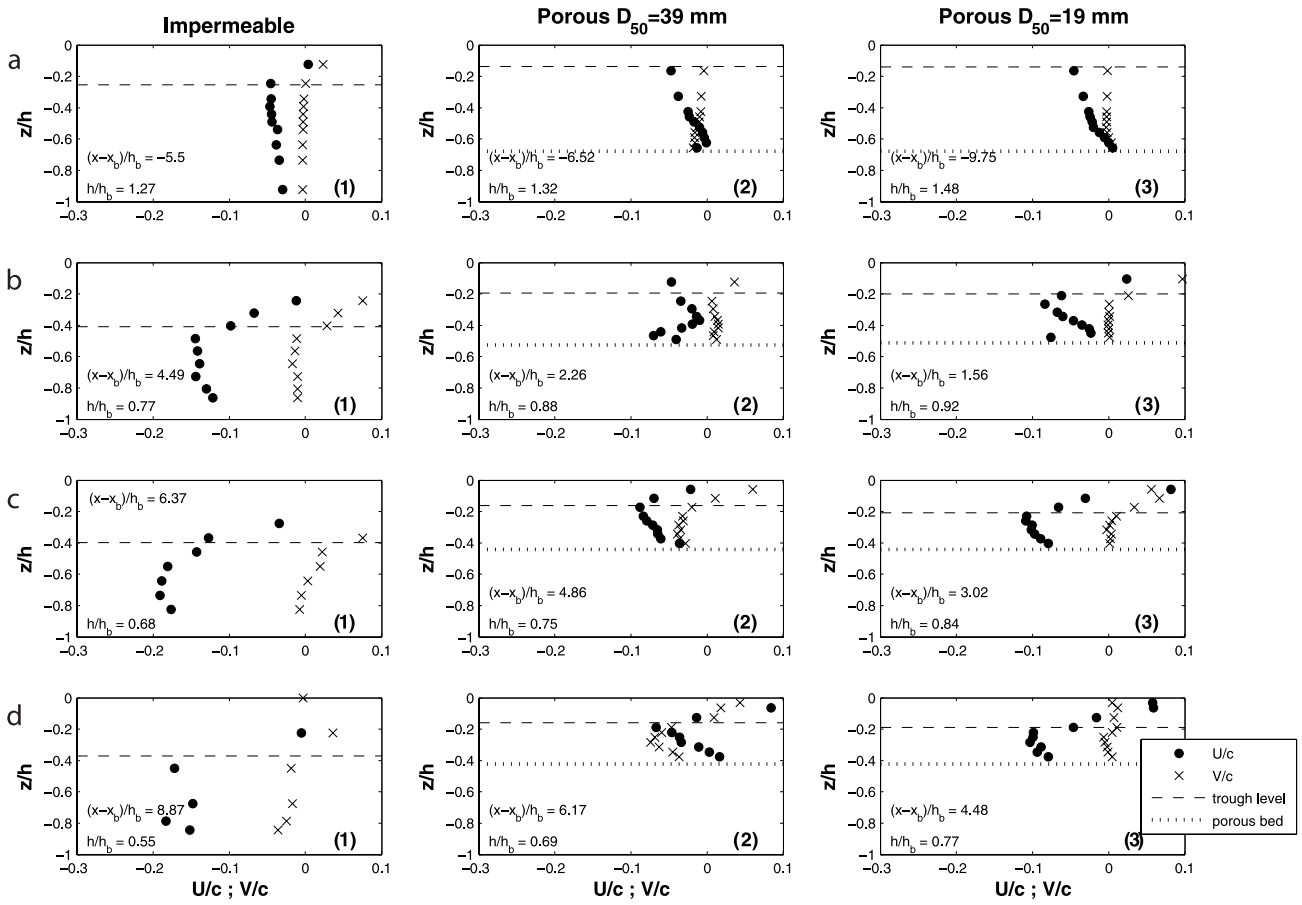

Figure 5. Normalized undertow (dots) and ensemble vertical velocity (crosses) for case L (H = 0.15 m, T = 4 s). Dashed line, trough level; dotted line, porous layer upper interface.

plotted in column, data at different locations along the surf zone are presented in row.

[28] Outside the surf zone, the turbulent velocities are small in comparison with the wave celerity. For the impermeable slope, the magnitude of turbulent velocity is around $10^{-3}c$, which is similar to that reported by *Ting and Kirby* [1994]. For a spilling breaker, turbulence is initially generated near the wave crest. Close to the breaking point in the outer surf zone (Figure 6b, plot 1), the surface roller is developing and turbulence levels are only significant above the wave trough level. Inside the surf zone, the horizontal turbulent component is always larger than the vertical component. Turbulence generated inside the roller is transported by advection toward the bed [*Peregrine and Svendsen*, 1978]. Turbulence velocities increase in the onshore direction and at the same time the breaker generated turbulence decreases with depth (plot 1 in Figures 6c and 6d).

[29] The turbulence generation processes over a gravel slope differ from those over an impermeable slope. Outside the surf zone, turbulence is generated above the gravel slope (see Figure 6a, plots 2 and 3). Visual observations indicated that flows over gravel slope are clearly turbulent and three-dimensional. Larger turbulence velocities are found at the bottom and decrease with distance from the bottom. The maximum horizontal and vertical turbulence components have similar magnitudes ($u' \sim v' \sim 0.02c$) above the gravel slopes.

[30] The analysis of the turbulent velocity components inside the surf zone provides substantial details of the turbulent flow characteristics. The turbulent flow for the small size gravel slope (plot 3 in Figures 6b, 6c, and 6d) shows a similar pattern as that described for a smooth impermeable slope. Larger turbulence velocity values are observed at the wave trough level and decrease linearly with depth. The turbulent velocity also increases in the onshore direction. The vertical component appears to be smaller than the horizontal component inside the surf zone. Experimental data presented in Figure 6 show that the order of magnitude of the turbulent velocity is almost the same for the impermeable slope and the small gravel size slope. It is conjectured that wave breaking generated turbulence dominates and is not significantly affected by the presence of the gravel slope.

[31] Significant differences are found in the dynamics of turbulence in the surf zone for the case of larger gravel size slope. Close to the breaking point (Figure 6b, plot 2), large turbulence velocities are observed near the gravel slope. However, the turbulence generated from the free surface roller has not reached the bottom. Both turbulent velocity components are almost identical at this location. In the inner surf zone, the wave breaking generated turbulence interacts with the turbulence generated from the gravel slope, result-

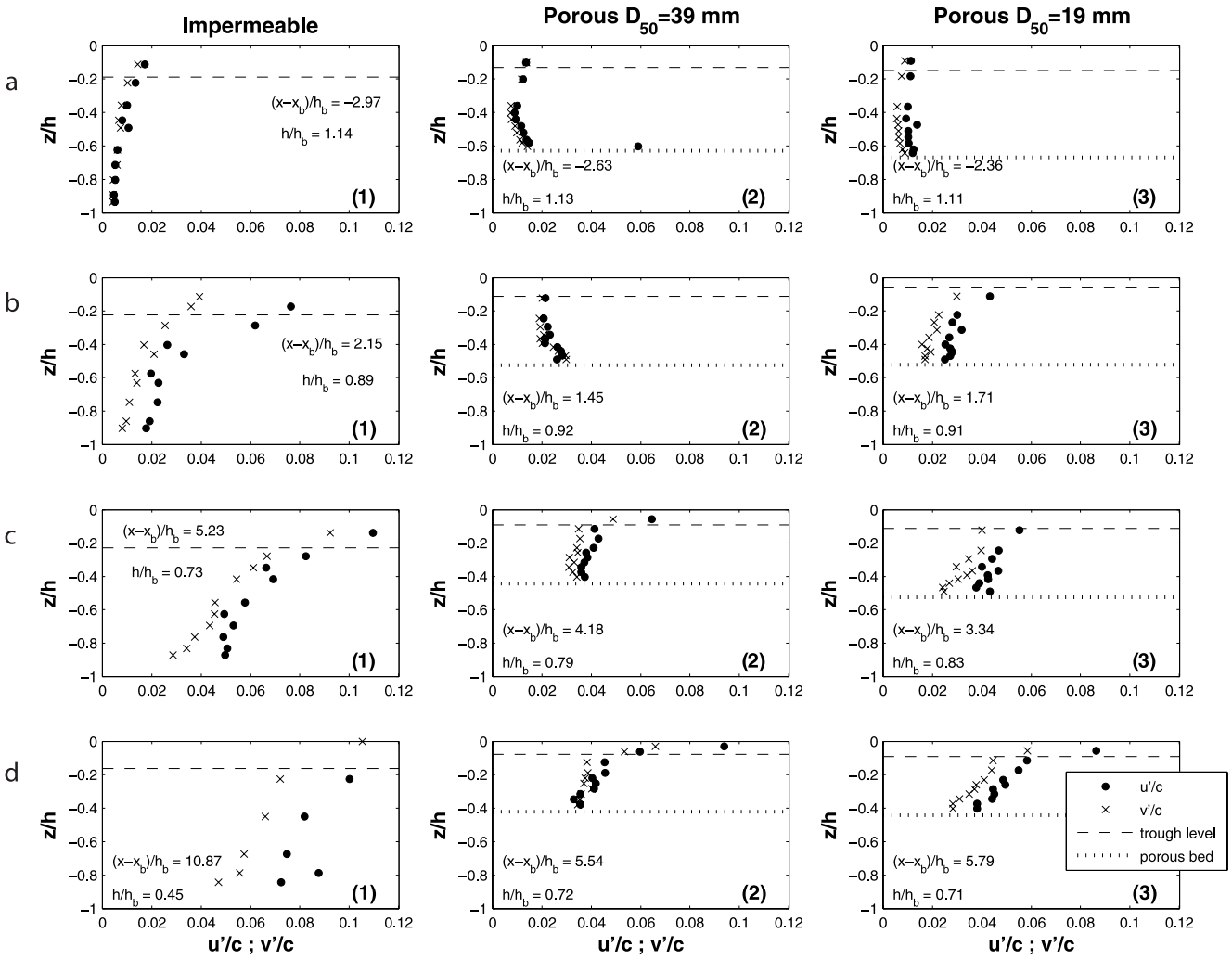

Figure 6. Normalized turbulence velocities: horizontal (dots) and vertical (crosses); for case F (H = 0.15 m, T = 2 s). Dashed line, wave trough level.

ing in weak vertical variation in turbulent intensities below the trough (plot 2 in Figures 6c and 6d), whereas, turbulence decreases more sharply from the free surface to the bottom in the other two cases. It is also important to point out that the turbulent velocities are in the same order of magnitude of the wave orbital velocities.

[32] Figure 7 shows the vertical profiles of horizontal and vertical components of turbulent velocities for a plunging breaker (case L, H = 0.15 m, T = 4 s). Previous works have reported the differences in wave breaking processes for the spilling and plunging breakers in terms of the way of turbulence generation by the breaker and the ratio of turbulence production-dissipation. At the breaking point, a tongue of water from the crest plunges into the oncoming flow and a violent transition to the rotational flow begins [*Ting and Kirby*, 1994]. Most of the energy is dissipated at this time because of the plunging of water. The horizontal turbulence velocity over an impermeable slope appears to be uniform with depth (plot 1 in Figures 7b, 7c, and 7d) and the magnitude of turbulence is stronger for plunging breakers. On the other hand, the vertical component decreases with depth in the surf zone. Measurements also show that horizontal components of turbulence are in general larger than the vertical component. This feature has not been reported in previous works.

[33] Turbulence characteristics for plunging breakers over the gravel beds are similar to those observed for the spilling breaker case. Outside the surf zone, turbulence is weak in the water column near the free surface. However, turbulence increases near the gravel slope. Inside the surf zone, turbulent velocities over the small-size gravel slope show similar patterns over the impermeable slope. Turbulence intensities decrease uniformly with depth, but increase slightly near the slope (plot 3 in Figures 7c and 7d). The horizontal turbulence velocity appears larger than the vertical turbulence velocity. Turbulence production above the gravel bed is not as significant as the turbulence production mechanism by wave breaking. The turbulence velocity magnitude appears smaller than that for the impermeable slope case because the ratio of wave height to the depth at breaker, $(H/h)_b$, related to the production and spreading of turbulence, is smaller for the small gravel size slope case.

[34] Turbulence patterns over the larger gravel size slope are different from those for other two slopes. Vertical and horizontal turbulent intensities are almost identical. Close to the breaking point (Figure 7b, plot 2), larger turbulent

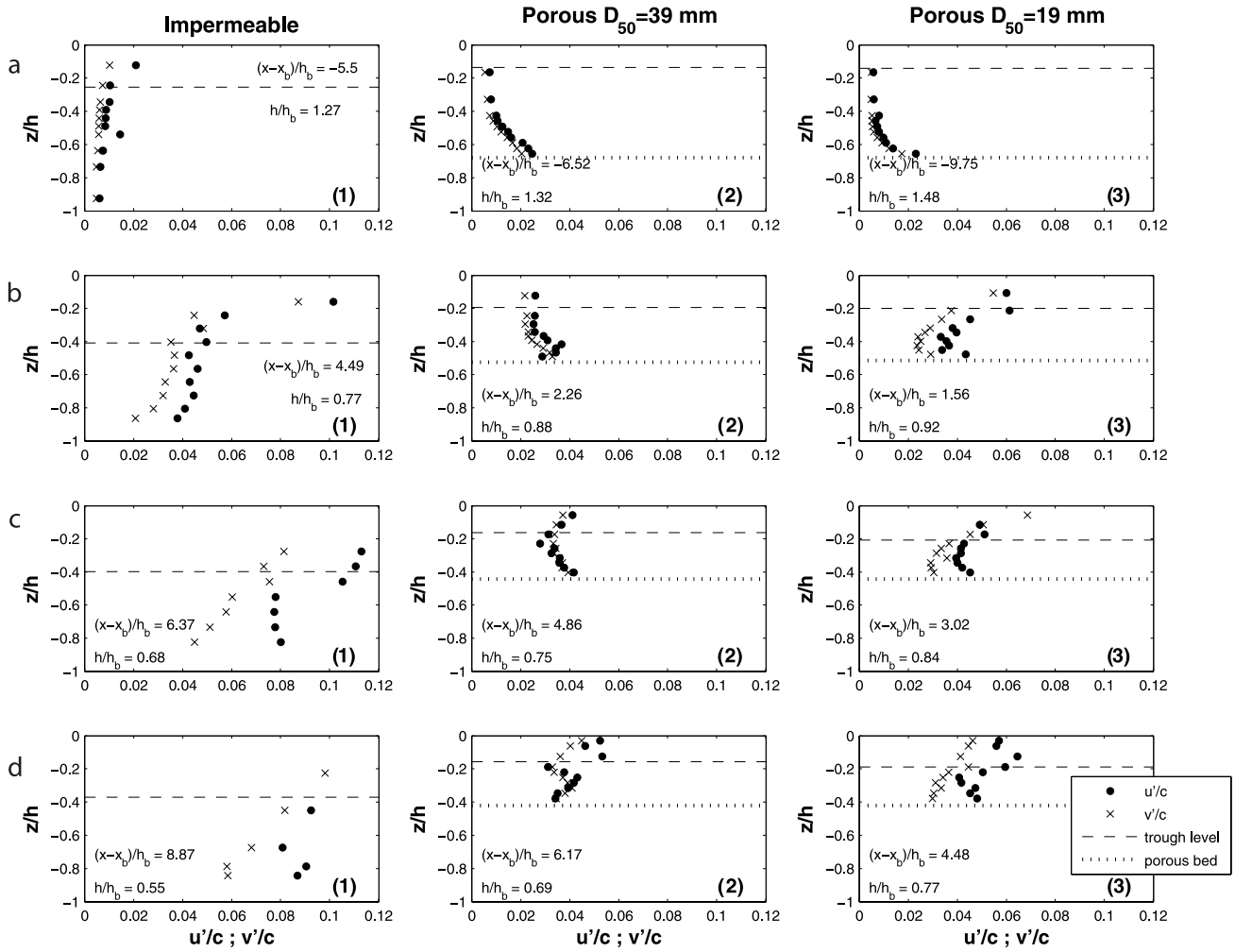

Figure 7. Normalized turbulence velocities: horizontal (dots) and vertical (crosses); for case L (H = 0.15 m, T = 4 s). Dashed line, trough level.

velocities are observed near the gravel slope. Turbulent velocities slightly increase in the onshore direction. In the inner surf zone, the turbulent velocities do not decrease monotonically. Moreover, time-mean velocities (plot 2 in Figures 5c and 5d) are of the same order. It is conjectured that the momentum mixing increases due to turbulent motions originated by the gravel slope. This effect increases the wave damping due to breaking compared to that over an impermeable bed.

4. Numerical Simulation

[35] In this section, the computational model, called COBRAS (COrnell BReaking waves And Structures), which is based on the Volume-Averaged Reynolds Averaged Navier-Stokes (VARANS) equations, is used to simulate the experiments. In this model a set of volume-averaged k-ε turbulence balance equations is employed to calculate the turbulent kinetic energy (k) and the turbulence damping rate (ε). The volume-averaged stress and volume-averaged strain rate are nonlinearly related through an eddy viscosity closure model. These model equations have been presented and discussed by *Hsu et al.* [2002], *Garcia et al.* [2004] and *Lara et al.* [2006] and hence they will not be repeated here. However, we remark here that in the VARANS equations, the interfacial forces between the fluid and solids have been modeled by the Forchheimer relationship, in which both linear and nonlinear drag forces are included. Two empirical coefficients, α and β, associated with the linear and nonlinear forces, respectively, are introduced. These coefficients should depend on the Reynolds number and the flow direction. We remark here that the inertia term is included in the VARANS equations. In the free fluid region above the gravel slope, the porosity, n, becomes unity, the VARANS equations and the volume-averaged k-ε turbulence balance equations reduce to the original RANS equations, *Lin and Liu* [1998a].

[36] In the numerical model, the two-step projection method is employed to solve the VARANS equations. The movement of free surface is tracked by the Volume of Fluid (VOF) method. Detailed discussions on the numerical algorithms and the initial and boundary conditions are referred to by *Lin and Liu* [1998a] and *Hsu et al.* [2002].

4.1. Numerical Setup

[37] The computational domain and the resolution of the mesh designed for the numerical simulations are sketched in

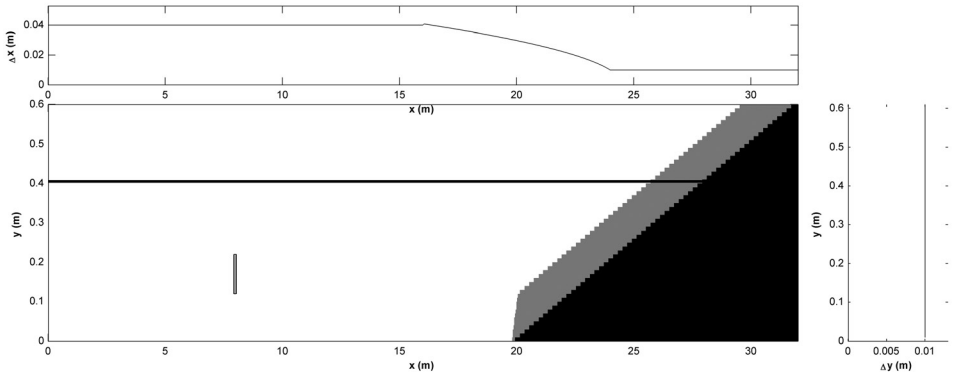

Figure 8. Sketch of computational mesh resolution.

Figure 8. An internal wave generator is used to generate the desired incident wave characteristics [*Lin and Liu*, 1999].

[38] The grid is uniform in the y direction with the grid size of 1 cm. In the x direction the cell size varies from 4 cm in the generation region to 1 cm in the vicinity of the gravel slope, which is the domain of interest. The total number of grids is 60 in the y direction and varies from 1518 for short waves up to 1764 in the case of the longest wave in the x direction.

4.2. Model Validation

[39] The first step of numerical simulations is to calibrate the empirical coefficients α and β. Although the values for α and β have been researched and recommended by several researchers [e.g., *Shih*, 1990; *van Gent et al.*, 1994; *van Gent*, 1995; *Burcharth and Andersen*, 1995; *Hsu et al.*, 2002; *Garcia et al.*, 2004] for surface piercing breakwaters, they need to be re-calibrated for the present experimental setups.

[40] We find the best fit values for α and β by comparing experimental data and numerical results of free surface displacement, bottom pressure below the gravel, and turbulent kinetic energy at different sections along the flume for case F with a D_{50} = 39 mm gravel slope. Thirty waves were numerically generated for each simulation. However, only the last 20 waves were used to compare with the measurements. The numerical results reached the quasi steady state within ten waves.

[41] An additional parameter affecting the inertia term in the extended Forchheimer model is included in the formulation. However, some preliminary runs have shown that results are almost insensitive to its variation. Therefore, for all the runs, this parameter has been kept constant. A value of 0.34 has been set on the basis of previous recommendations.

[42] After several trials and errors, the best-fit parameter values are: α = 200 and β = 0.2. We remark that numerical results are more sensitive to the nonlinear drag coefficient β than the linear drag parameter α, because the flow is mainly turbulent, especially at the upper portion of the gravel bed. Once these parameters are determined, they are kept as constants in the rest of the analyses.

4.3. Gravel Slope With D_{50} = 39 mm

[43] Numerical results for both spilling and plunging breakers over the gravel slope with D_{50} = 39 mm are presented in this section. Comparisons between the experimental data and numerical solutions are also discussed. In Figure 9 the upper ($\eta_{\max} - \eta_{mean}$) and lower ($\eta_{\min} - \eta_{mean}$) wave envelopes and the mean free surface level (η_{mean}) for case F (H = 0.15 m, T = 2 s) are compared with laboratory measurements. The overall agreement between the numerical results and the experimental data is very good. The shoaling pattern and the breaking point location are accurately reproduced by the numerical model. However, discrepancies are more significant near the breaking point, which can be attributed to the fact that: (1) air bubbles, generated through the breaking process, could result in less accurate wave gauge measurements and (2) the numerical model has entirely neglected the air bubble dynamics. In the inner surf zone, the role of the air bubbles is less significant and the numerical results show a better agreement with experimental data. We note that the last three gauges are actually embedded inside the gravel slope within the gravels (see Figure 1). At these locations, both envelopes and mean water level calculated by the model agree very well with the data.

[44] The calculated time histories of the free surface displacement at fifteen locations are compared with laboratory measurements in Figure 10. The breaking point is located between gauges 11 and 12 (Figure 10, plots 3 and 4). Since the wave generation method used in the laboratory experiment differs from that employed in the numerical model, the reference time for comparison is fixed by matching the time histories of the numerical solutions and experimental data at the gauge 1, located 3.5 m offshore the toe of the slope on the horizontal bottom region.

[45] The overall agreement between the experimental data and the numerical results for the free surface fluctuations is excellent. In the surf zone, the instantaneous saw-tooth shape surface profiles for broken waves are accurately simulated. We should also point out that in the swash zone the water depth is smaller than the thickness of the gravel slope. Thus, as mentioned before, the measurements at wave gauges 23, 24 and 25 in Figure 10 represent the surface displacements inside the gravel slope. The excellent agreement between the numerical results and experimental data at these sections indicates that flows inside the gravel slope are modeled properly.

[46] To further validate the model, the comparison of time histories of the dynamic pressure on the Plexiglas underneath the gravel slope for a plunging breaker case

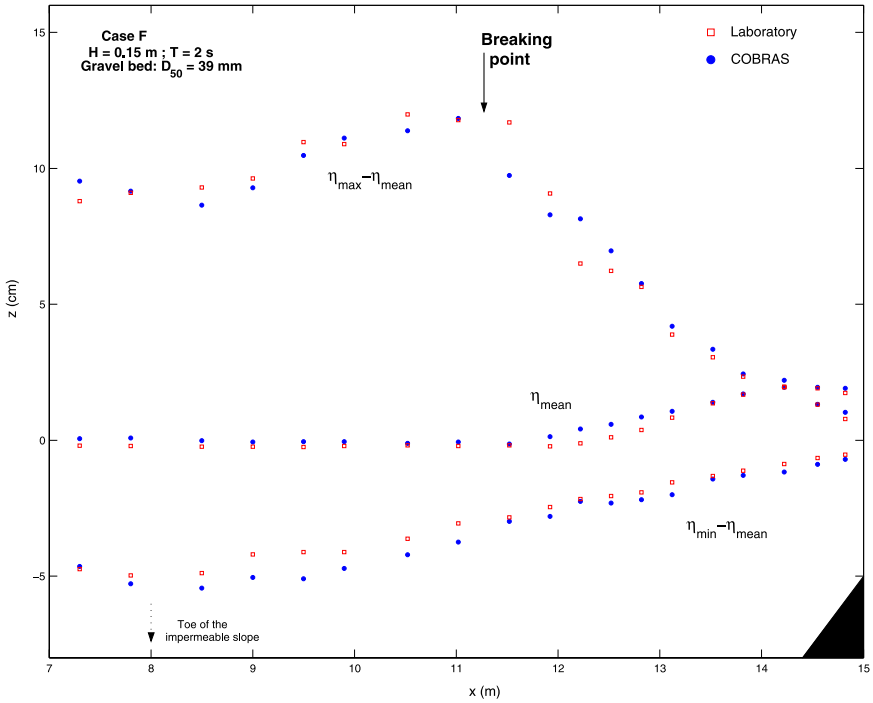

Figure 9. Distribution of mean water level, upper and lower envelopes for case F ($H = 0.15$ m, $T = 2$ s) for a $D_{50} = 39$ mm gravel slope for laboratory results and numerical modeling.

(case I: $H = 0.15$ m, $T = 3$ s) at different sections is shown in Figure 11. We remark that the same parameter values, $\alpha = 200$ and $\beta = 0.2$, are adopted for this case. Figure 11 (top) shows results at a location seaward of the breaking point and the rest of the panels correspond to sections inside the surf zone. Only small differences are observed between the calculated pressures and the experimental data.

[47] Figures 12 and 13 show the comparisons between measurements and numerical simulations of the time histories of the horizontal and vertical velocities at two vertical cross sections within the surf zone for spilling and plunging breakers, respectively. At each location, 10 waves are presented at eight different elevations below the wave trough. The overall agreement for the horizontal velocity components in the spilling breaker case is very good (Figure 12). The nonlinear wave patterns are simulated accurately. The data/model agreement for the vertical velocity component is not as good as that for the horizontal velocity component. The numerical model seems to underestimate the percolation flows into the gravel slope.

[48] At the locations near the gravel slope, local effects due to bottom irregularity are visible in the experimental data. High-frequency fluctuations are observed in the experimental measurements and the complex flows over the gravel slope are in general three-dimensional. Therefore, the 2-D spatially averaged numerical model is not capable of simulating the details. Nevertheless, for locations near the still water level where the local bottom induced flows are less important, the numerical calculations agree much better with the experimental results.

[49] Figure 13 displays the time histories of the velocity components for the plunging breaker (i.e., case I) at $(x - x_b)/h_b = 3$. At this cross section, the still water depth above the gravel slope is almost the same as the thickness of the gravel slope. The shape of the horizontal velocity components reveals a small "hump" trailing the wave crest. The numerical model is able to simulate the time histories of the horizontal velocity in detail, including the trailing hump.

[50] The vertical velocities are also very well reproduced by the model near free surface, capturing the vertical velocity magnitudes. Similar to the spilling wave case, high frequency velocity oscillations are observed in the experimental data but not in the numerical calculations.

[51] The comparisons of undertow for case F and I are presented in Figures 14 and 15, respectively. Comparisons are shown for 8 locations; four outside the surf zone and four within the surf zone. Undertow is calculated numerically by taking a time average of the horizontal velocity results over 20 waves after the numerical solution has reached the quasi steady state. Agreements are very good at locations outside the surf zone for both types of breakers. However, some discrepancies are observed at elevations close to the bed. Figures 14b and 15b and Figures 14d and 15d in both cases show that the numerical results underestimate the undertow magnitudes near the gravel slope. Inside the surf zone comparisons are also good at several locations (i.e., Figures 14e, 14f, 15e, and 15f). However, for the locations where the water depth is almost the half of the gravel bed thickness (i.e., Figures 14g, 14h, 15g, and 14h), the model is not able to simulate correctly the measured undertow, especially for the plunging breaker, that generates higher velocity values over the gravel. This is caused because the wave flow over the bed is strongly influenced by the shape and the position of the gravel being mainly three-dimensional and the model cannot capture the details of the flow motions generated over the gravel slope. The bottom geometry definition in the numerical modeling is

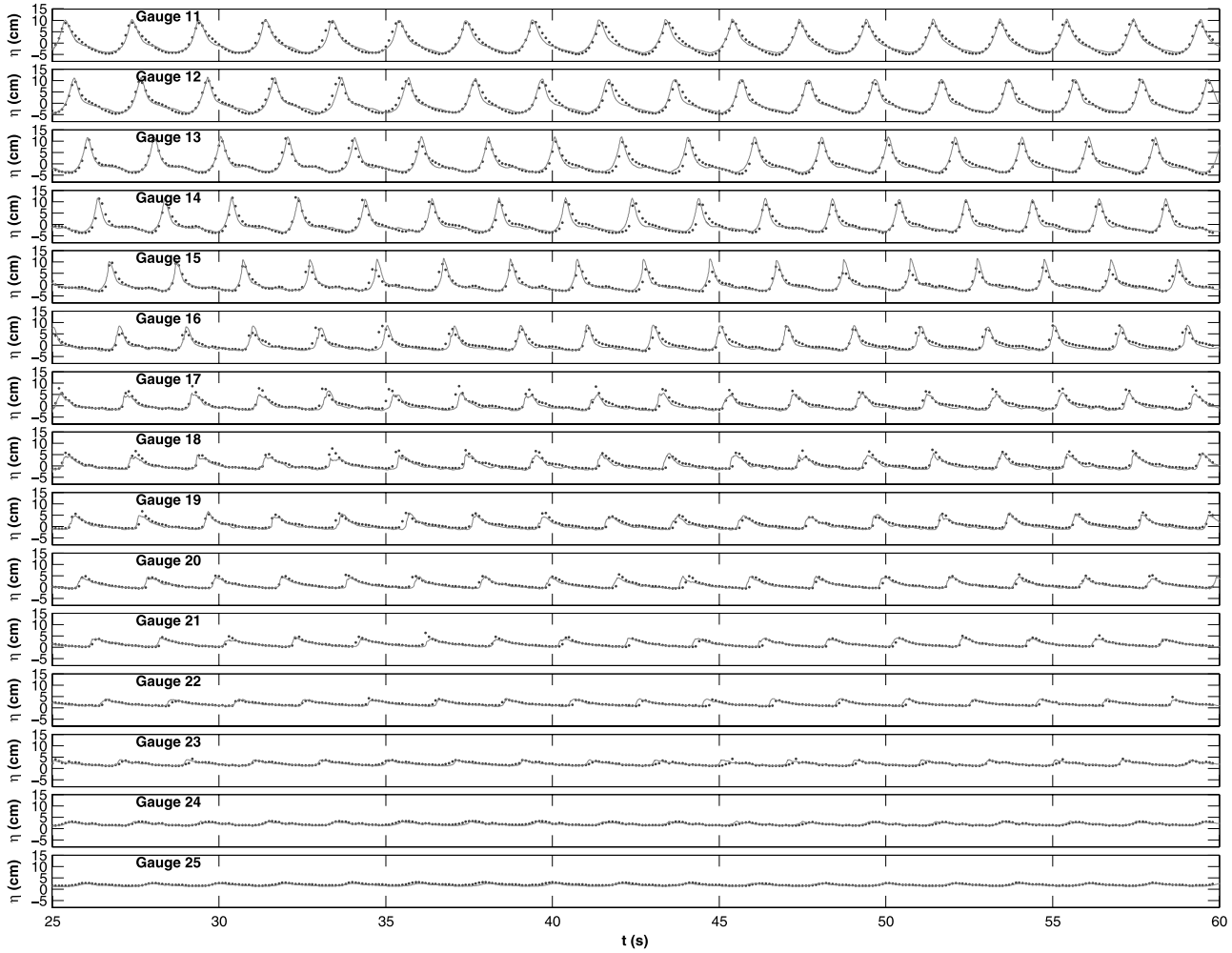

Figure 10. Comparisons of free surface time history for case F (H = 0.15 m, T = 2 s) and for a D_{50} = 39 mm gravel size slope between numerical results (dots) and laboratory experiments (dashed line) for different locations.

different from that of the experiments. The individual stones are not considered in solving the equations.

[52] In the top four plots of Figure 16 the dimensionless time-mean turbulent intensity inside the surf zone is shown for a plunging breaker (case I, H = 0.15 m, T = 3s D_{50} = 39 mm). The bottom plots in Figure 16 display the phase averaged horizontal and vertical velocities and the turbulent intensity at a cross-section within the surf zone ($(x - x_b)/h_b = 5.5$). At this location, comparisons are made at eight different elevations below the wave trough. The first and second rows of Figure 16 correspond to horizontal and vertical velocities, respectively, and the third row represents the turbulent intensity. The eight columns correspond to different elevations of measurement points. The distance has been normalized with the local water depth and is specified at the top of each plot of the first row. Experimental data are plotted in grey lines and numerical results in black lines. The magnitudes of the velocity field are obtained by phase-averaging over twenty waves for both the numerical results and the experimental data. Since only two components of turbulence velocities were measured by LDV, the total turbulent kinetic energy was estimated by the empirical formula after *Svendsen* [1987], i.e., $k = \frac{2}{3}(u'^2 + v'^2)$, where u' and v' are turbulence velocities in the horizontal and vertical direction, respectively. This procedure was also employed by *Lin and Liu* [1998a, 1998b], although some uncertainties may be introduced in the results for turbulence.

[53] The overall agreement between the experimental data and the numerical results of the phase averaged velocity components is reasonable as shown in Figure 16. The numerically calculated velocities describe quite well the phase evolution pattern observed in the experiments in the whole water column. However, numerical results overestimate both horizontal and vertical velocities under the wave crest. Similar results were obtained by *Lin and Liu* [1998a] over an impermeable slope. It is conjectured that the discrepancies between the experiments and the numerical calculations are due to the air entrainment by the roller at the crest phase that affects the velocity measurements. At the locations close to the bottom, local effects due to bottom irregularity become visible in the experimental data, in particular for the vertical velocity. Velocity fluctuations with a period smaller than the wave period are observed in the experimental measurements under the wave trough as the flows moves in the offshore direction. The complex flows

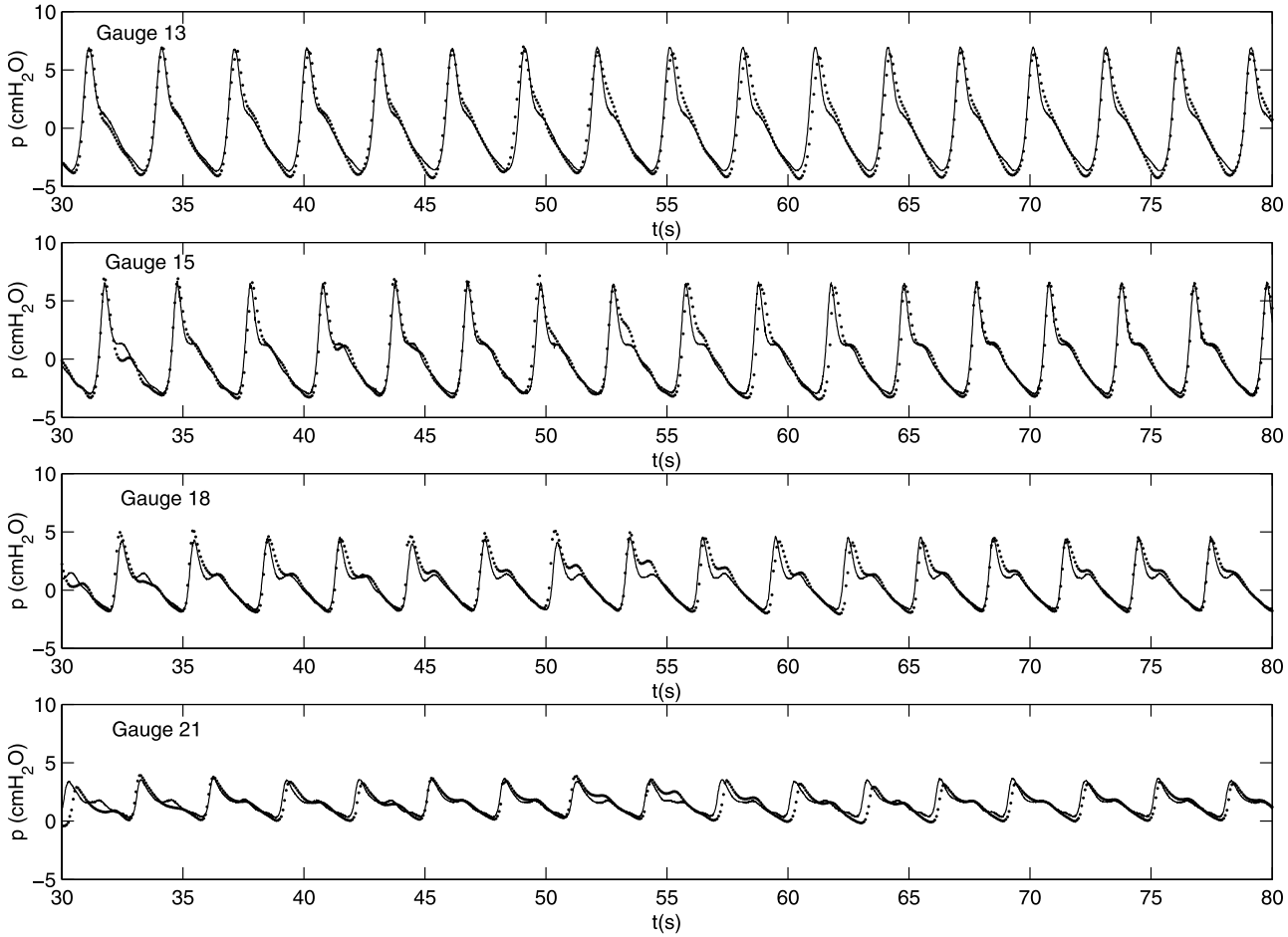

Figure 11. Comparisons of dynamic pressure time history for case I (H = 0.15 m, T = 3 s) and for a D_{50} = 39 mm gravel size slope between numerical results (dots) and laboratory experiments (dashed line) for different locations.

over the gravel slope are in general three-dimensional and therefore the numerical model is not capable of simulating the details. Nevertheless, for positions near the still water level where the local bottom induced flows are less important and the numerical calculations for vertical velocity agree much better with the experimental results.

[54] Previous numerical research results such as those of *Lin and Liu* [1998a, 1998b] and *Hsu et al.* [2002] have shown that time-mean TKE is, in general, numerically overestimated. The four top plots in Figure 16 also show the same feature. At the outer surf zone (two top plots), the model clearly overestimates experimental measurements. In the first plot, which is close to the breaking point, the breaking-wave generated turbulence has not penetrated the whole water column; experimental results show larger turbulent intensity close to the bottom. The numerical model is not able to reproduce this feature and numerically calculated turbulence intensity shows the same patterns as those in the inner surf zone. A careful analysis of the numerical calculations at the outer surf zone has revealed that most of the turbulence at that region is advected offshore by the undertow. The k-ε turbulence model used for the computations is not able to generate enough dissipation to reduce turbulence outside of the surf zone.

[55] Phase-averaged turbulent intensity is presented at the bottom row of Figure 16. Results show that the turbulent intensity values for experimental and numerical data are very close in magnitude below the wave trough. Only the maximum turbulent intensity that is in phase with the maximum horizontal velocity is overestimated. However, near the gravel slope, the time evolution of turbulent intensity calculated by the model differs from the experimental results. It is conjectured that the wave flows over the bed is strongly influenced by the shape and position of each individual gravel and can not be modeled by the present model.

4.4. Gravel Slope With D_{50} = 19 mm

[56] Numerical results for spilling and plunging breaker over a gravel slope with D_{50} = 19 mm gravel size are presented in this section.

[57] Figures 17 and 18 display numerical results and experimental data for the free surface time histories of case F. The location of the wave breaking point is between gauges 13 and 14. Overall, the numerical model is able to predict reasonably well the wave breaking process over the gravel slope with smaller gravel size. Again the differences between the numerical and experimental results are observed in the aerated regions (gauges 16, 17 and 18)

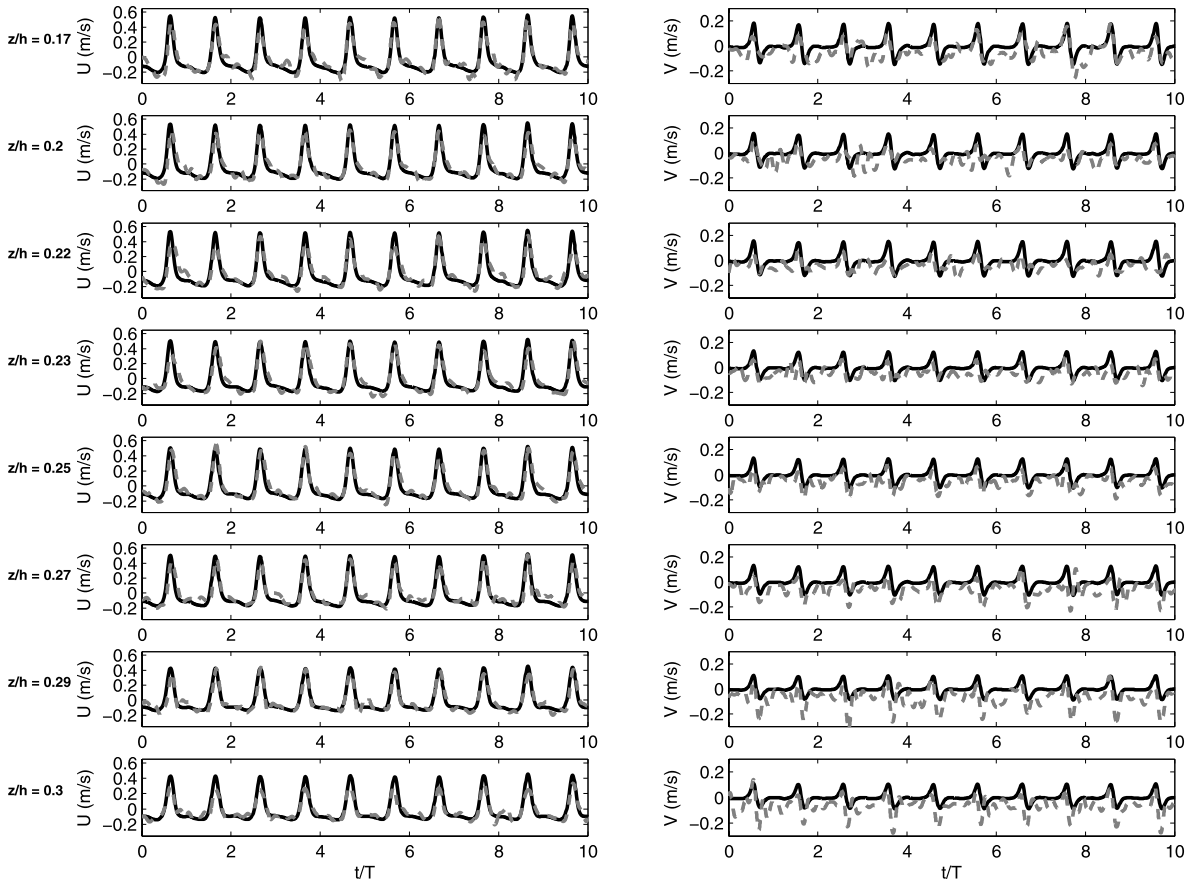

Figure 12. Comparisons between numerical results (solid line) and laboratory experiments (dashed line) of horizontal and vertical velocity time history for case F (H = 0.15 m, T = 2 s) and for a D_{50} = 39 mm gravel size slope at $(x - x_b)/h_b = 2.81$.

where the numerical model overestimates the free surface elevation. In the rest of surf zone, the waveshape and the wave amplitude are very well reproduced by the numerical model. In the inner surf zone, the calculated time history of free surface shows slight phase shifts for a few waves in the record.

[58] Figure 19 presents the comparisons of numerical results and experimental data for the time history of dynamic pressure below the gravel slope for case F. The four plots represent four locations inside the surf zone. The characteristics and magnitudes of the pressure fluctuations are similar to those observed for the case with a larger gravel size (i.e., Figure 11). However, in this case because of the reduction of the seepage velocity, the time history records show lower energy content for the second and third harmonics; that is, the pressure variations in time are relatively smooth without obvious secondary peaks. Apparently, the energy dissipation increases for the gravel slope with smaller gravel size.

[59] Figures 20 and 21 show the comparisons of experimental data and numerical results for the time histories for horizontal and vertical velocities at two vertical cross sections within the surf zone for spilling and plunging breakers, respectively. The overall agreement for the horizontal velocity, shown in Figure 19 for the spilling breaker, is very good. However, numerical results overestimate slightly at elevations closer to the still water level. The degree of data/model agreement for the vertical velocities is lower than that for the horizontal velocities. For the small gravel size, weaker influence of the gravel slope on the velocity field can be seen in the entire water column. In fact, measured horizontal velocities near the gravel bed agree very well with the calculated data. Furthermore, the numerical model is able to reproduce the percolation velocity at the gravel bed.

[60] For the plunging breaker (Figure 21), the numerical results also agree very well with laboratory data. The velocity field comparisons are improved over those for the case of gravel slope with a larger gravel size. The typical horizontal velocity sawtooth shape within the surf zone is accurately reproduced. The model also accurately estimates the percolation velocity. Although the individual stones geometry is not considered in the numerical model, the model produces very reasonable velocity patterns over the gravel bed.

[61] Figure 22 shows the normalized time-mean turbulent intensity and normalized phase-averaged velocities and turbulent intensity for case I ($(x - x_b)/h_b = 7.11$), respectively. The overall agreement for the phase-averaged velocity components between the experimental data and the numerical results is very good. Because of the weaker influence of the gravel slope, the calculated mean vertical velocities display a much better agreement with the measured data. The typical sawtooth type shape of the horizon-

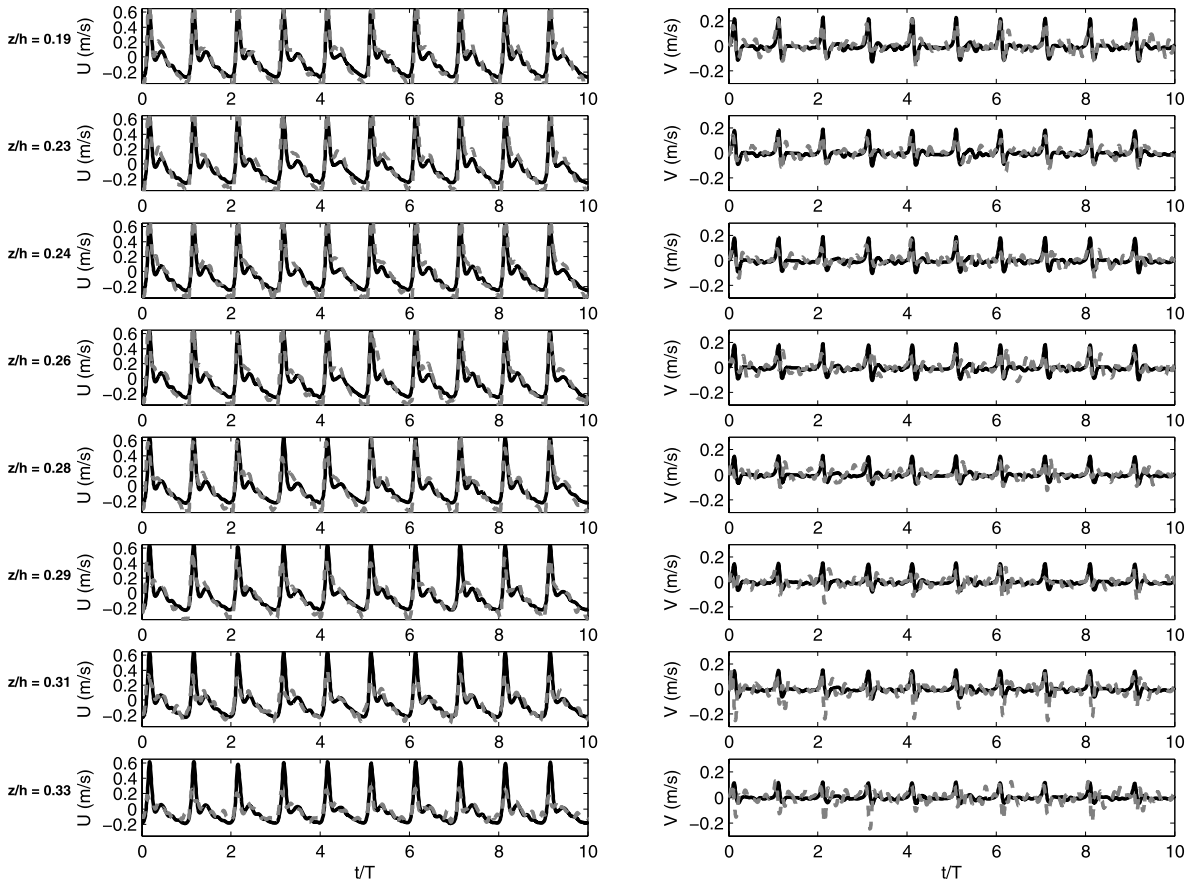

Figure 13. Comparisons between numerical results (solid line) and laboratory experiments (dashed line) of horizontal and vertical velocity time history for case I ($H = 0.15$ m, $T = 3$ s) and for a $D_{50} = 39$ mm gravel size slope at $(x - x_b)/h_b = 3$.

tal velocity is very well simulated by the model. The velocity field comparisons are improved over those for the case of gravel slope with a larger gravel size because the gravel influence on the flow is reduced with the mean gravel diameter. The model also reproduces very well the percolation velocity observed in the vertical velocity field.

[62] As was shown for the other gravel bottom case, time-mean turbulent intensity patterns simulated by the model overestimate the experimental values in the surf zone. However, the difference between numerical calculations and experimental results is reduced, because of the weaker influence of the gravel bed on the surf zone dynamics. Comparisons for the phase-averaged turbulent intensity demonstrate also a better agreement than for the larger gravel slope. The phase-averaged turbulent intensity at the wave trough is very well reproduced by the model. However, discrepancies are again observed at the wave crest phase and at locations close to the bottom. The decreasing with depth phase-averaged turbulent intensity for the eight presented locations is quite well simulated.

5. Conclusions

[63] To examine the effects of a gravel slope on the shoaling and breaking of water waves, a set of comprehensive laboratory experiments was performed, in which fluid velocities, pressure and water surface elevation were measured and analyzed. Measurements were made at cross sections inside and outside of the surf zone. Experiments for gravel slopes being made of two different gravel sizes were conducted for twelve wave conditions, covering both spilling and plunging breakers. Using the experimental data, the numerical model, based on VARANS equations with volume-averaged k-ε balance equations, is calibrated and validated.

[64] The following main conclusions can be drawn from this investigation.

[65] 1. The appearance of the gravel slope affects the shoaling and wave breaking processes significantly. The gravel slope provides an energy dissipation mechanism in the shoaling region, resulting in different breaker locations, breaker types and mean water level evolution.

[66] 2. Inside the surf zone, the mean free surface setup over a gravel slope is higher than that over an impermeable slope. The setup increases with increasing gravel size.

[67] 3. The magnitude of the undertow is smaller under waves propagating over a gravel slope. In the outer surf zone, the undertow under spilling breakers has a maximum value near the wave trough and decreases with water depth. Close to the bottom, the undertow decreases faster. In the inner surf zone, the undertow becomes more uniform throughout the entire water column and the vertical time-mean velocity increases. The influence of a gravel slope is greater for the larger gravel size under spilling breakers. The

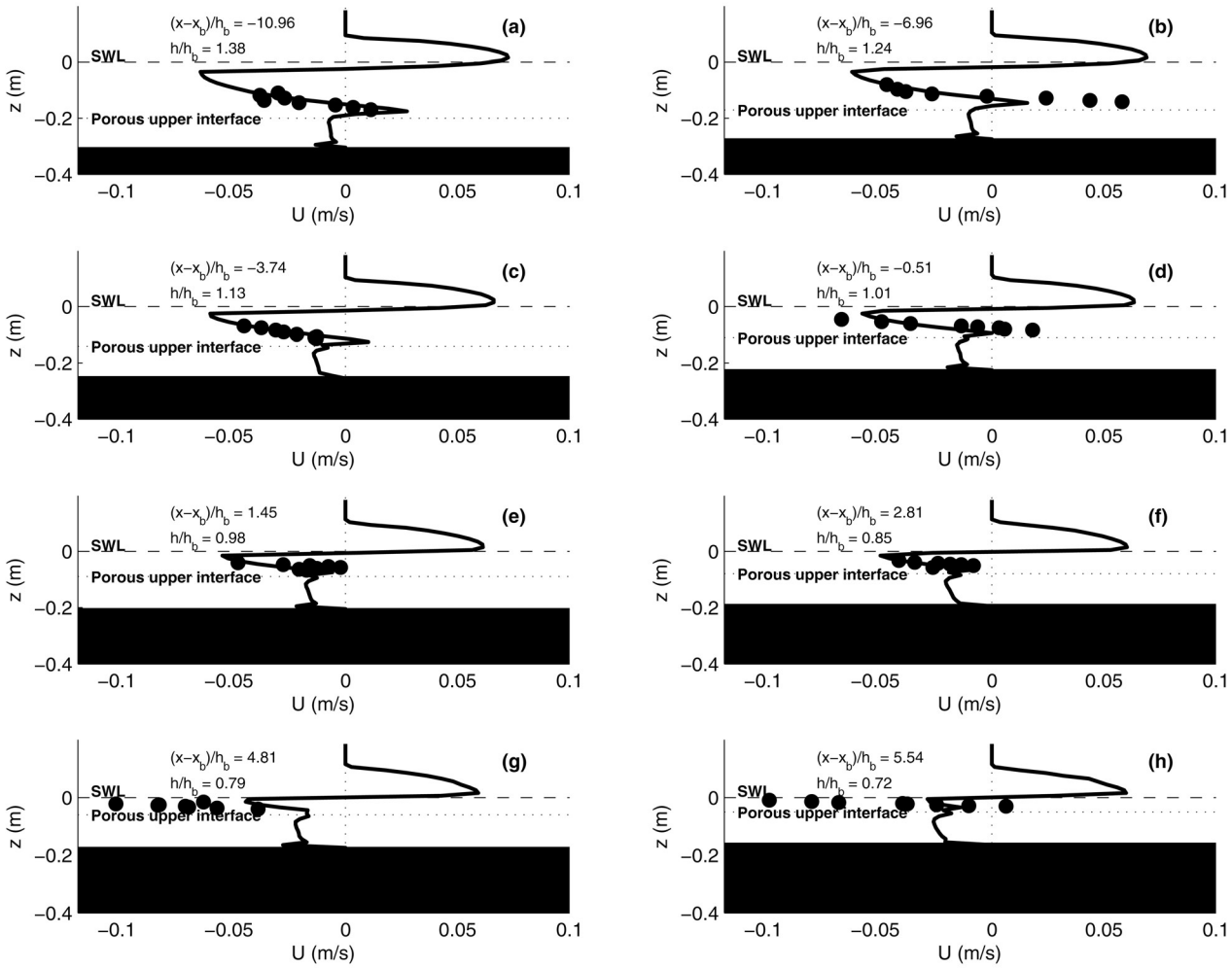

Figure 14. Comparisons of undertow for case F (H = 0.15 m, T = 3 s) and for a D_{50} = 39 mm gravel between numerical results (solid line) and laboratory experiments (dots) for different locations.

smaller gravel size shows patterns similar to the impermeable slope. The vertical distribution of undertow for plunging breakers is similar to that of the impermeable slope case within the outer surf zone and at the beginning of the inner surf zone. Close to the shoreline, the vertical time-mean velocity grows and the undertow profile is highly affected.

[68] 4. Under the influence of a gravel slope, the turbulence velocity pattern in the shoaling zone differs from the impermeable slope case. The turbulence intensity is very small just below the wave trough. However, turbulence velocities reach a maximum value above the gravel bed. Within the outer surf zone the spilling breakers show two different turbulence sources: broken wave generated turbulence below the trough level and wave motion induced turbulence over the gravel slope. Near the breaking point, turbulence velocities are dominated by wave breaking generated turbulence. While horizontal turbulent velocities appear predominant in the breaking process, horizontal and vertical turbulent velocities are in the same order of magnitude near the gravel bed. The gravel-slope generated turbulence is less importance in the case of plunging breaker.

[69] 5. The overall agreement between the experimental data and the numerical simulation results for the free surface time history, wave envelope, mean water level, velocities and undertow is reasonable. Free surface elevation is slightly underestimated close to the breaking point. Presumably, this is caused by the fact that some physical processes, such as the presence of air bubbles, have not been taken into account in the model. The model is able to reproduce very well the velocity field under broken waves on a different gravel slope characteristics. Time history records and undertow comparison have revealed a high degree of agreement. Horizontal velocities are correctly calculated for the model for any breaking type or any bottom characteristics. Larger discrepancies in velocity calculations are observed over gravel bed. The wave flow over the bed is strongly influenced by the shape and the position of the gravel and the model cannot capture the details of the flow motions generated over the gravel slope. The bottom geometry definition in the numerical modeling is different from that of the experiments. The individual stones are not considered in solving the equations. The weaker influence of the smaller gravel bed on the flow yields on an improvement of the computational results, especially on the vertical velocities. Undertow is also very well reproduced by the model, not only outside the surf zone but also within the surf zone. The model is able to reproduce phase-averaged

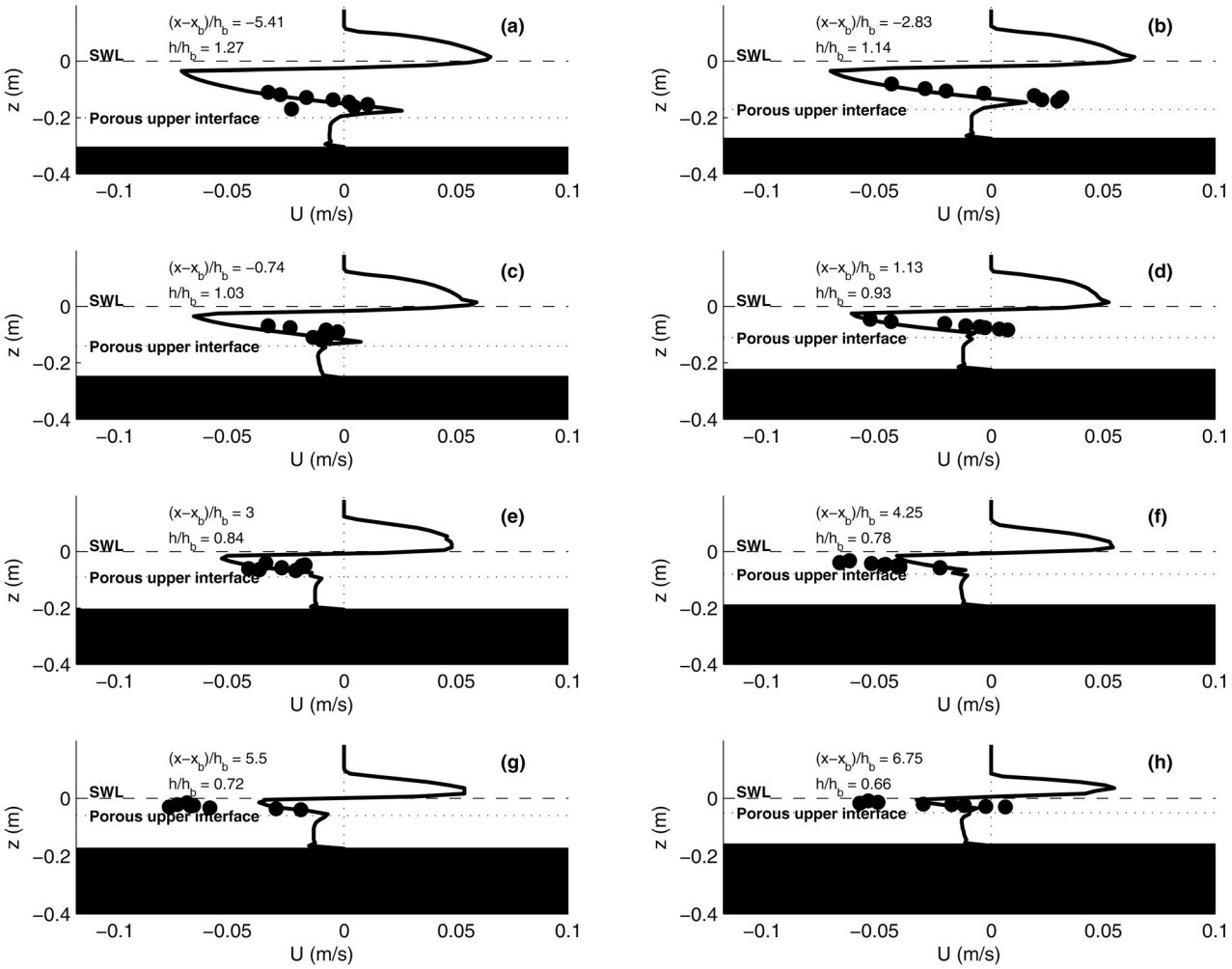

Figure 15. Comparisons of undertow for case I (H = 0.15 m, T = 3 s) and for a D_{50} = 39 mm gravel between numerical results (solid line) and laboratory experiments (dots) for different locations.

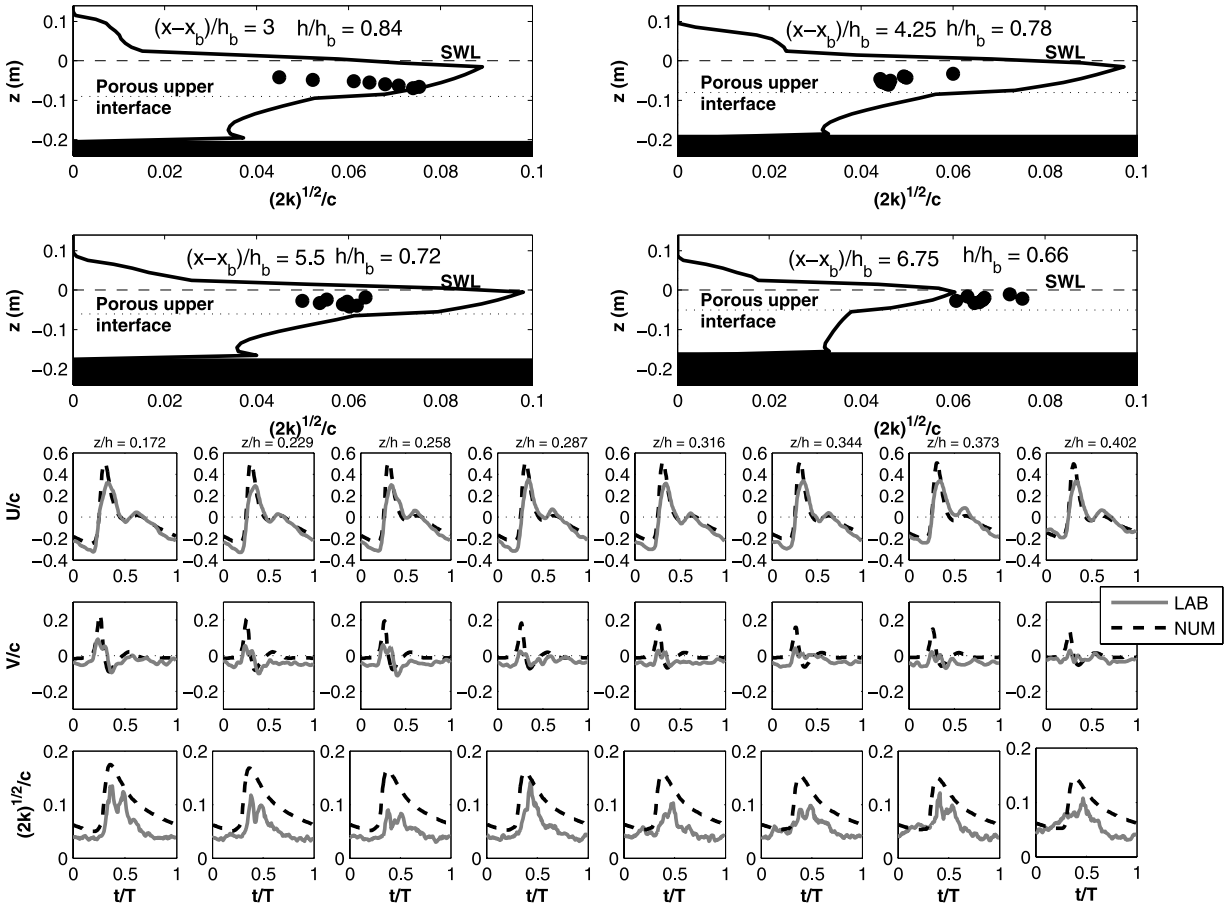

Figure 16. (top four plots) Comparisons between numerical results (solid line) and laboratory experiments (dots) for dimensionless time-mean turbulent intensity for case I ($H = 0.15$ m, $T = 3$ s) and for a $D_{50} = 39$ mm gravel for different locations. (bottom plots) Comparisons of phase averaged magnitudes for normalized horizontal velocity (top row), normalized vertical velocity (middle row), and normalized turbulent intensity (bottom row) at $(x - x_b)/h_b = 5.5$ for case I ($H = 0.15$ m, $T = 3$ s) for a $D_{50} = 39$ mm gravel size bed.

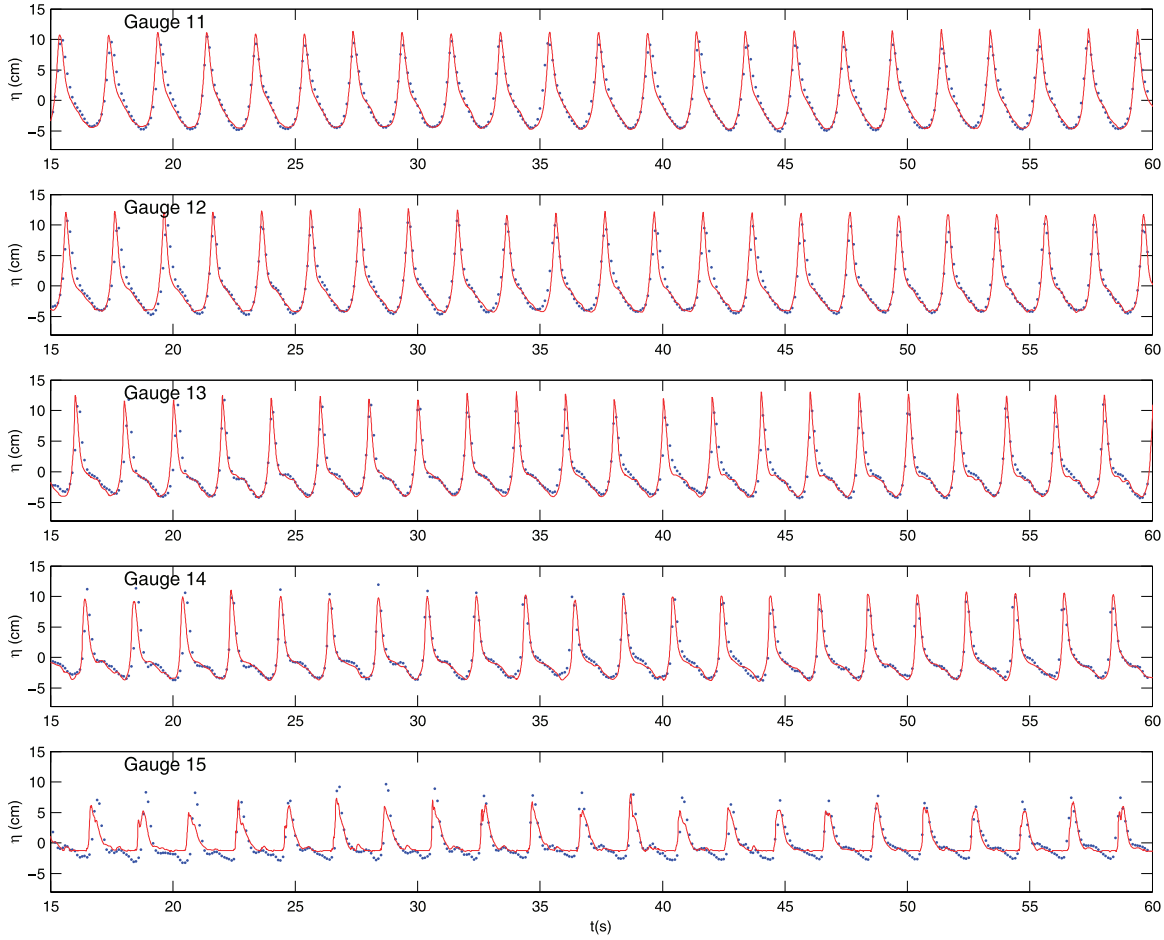

Figure 17. Comparisons of free surface time history for case F (H = 0.15 m, T = 2 s) and for a D_{50} = 19 mm gravel size slope between numerical results (dots) and laboratory experiments (dashed line) for different locations.

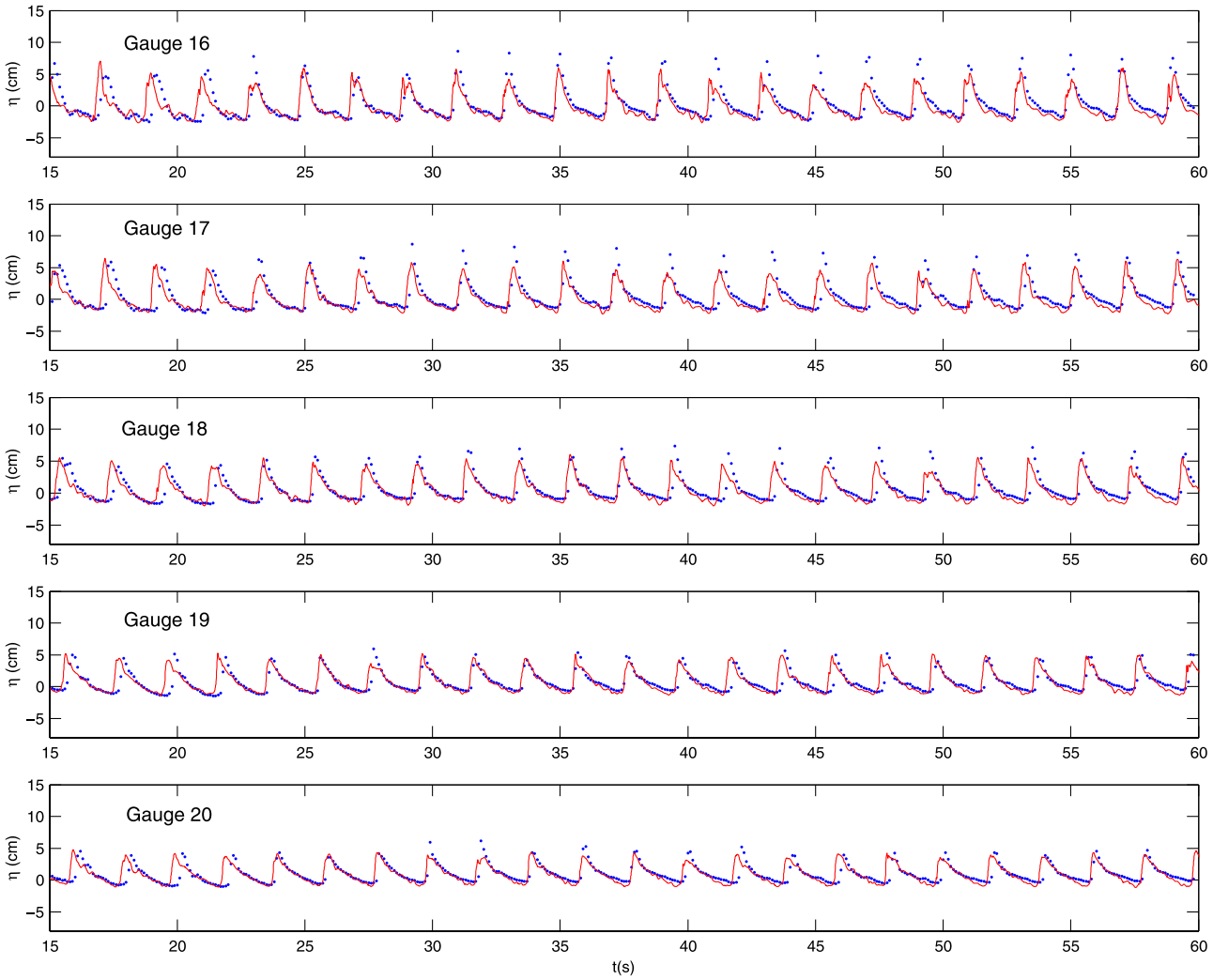

Figure 18. Comparisons of free surface time history for case F ($H = 0.15$ m, $T = 2$ s) between numerical results (dots) and laboratory experiments (dashed line) for different locations.

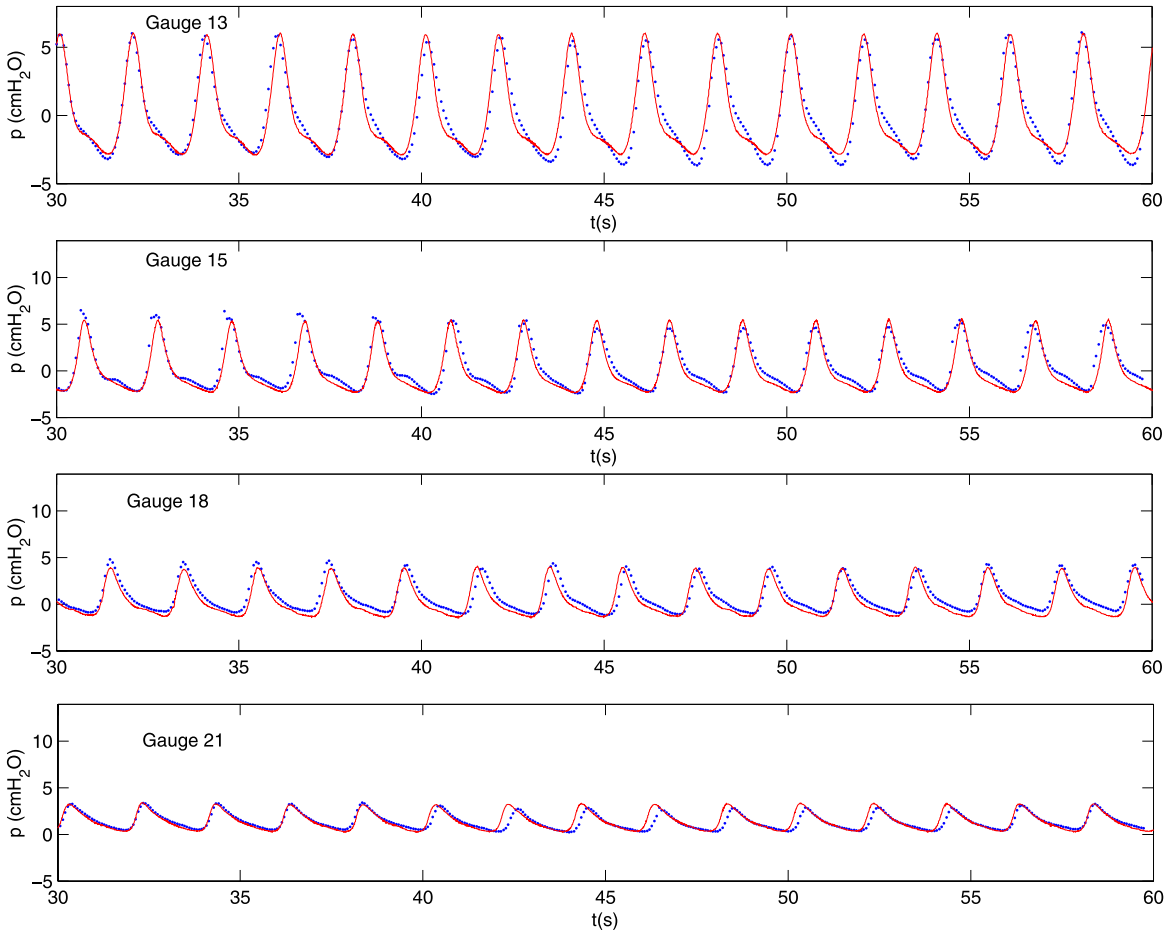

Figure 19. Comparisons of dynamic pressure time history for case F (H = 0.15 m, T = 2 s) and for a D_{50} = 19 mm gravel size slope between numerical results (dots) and laboratory experiments (dashed line) for different locations.

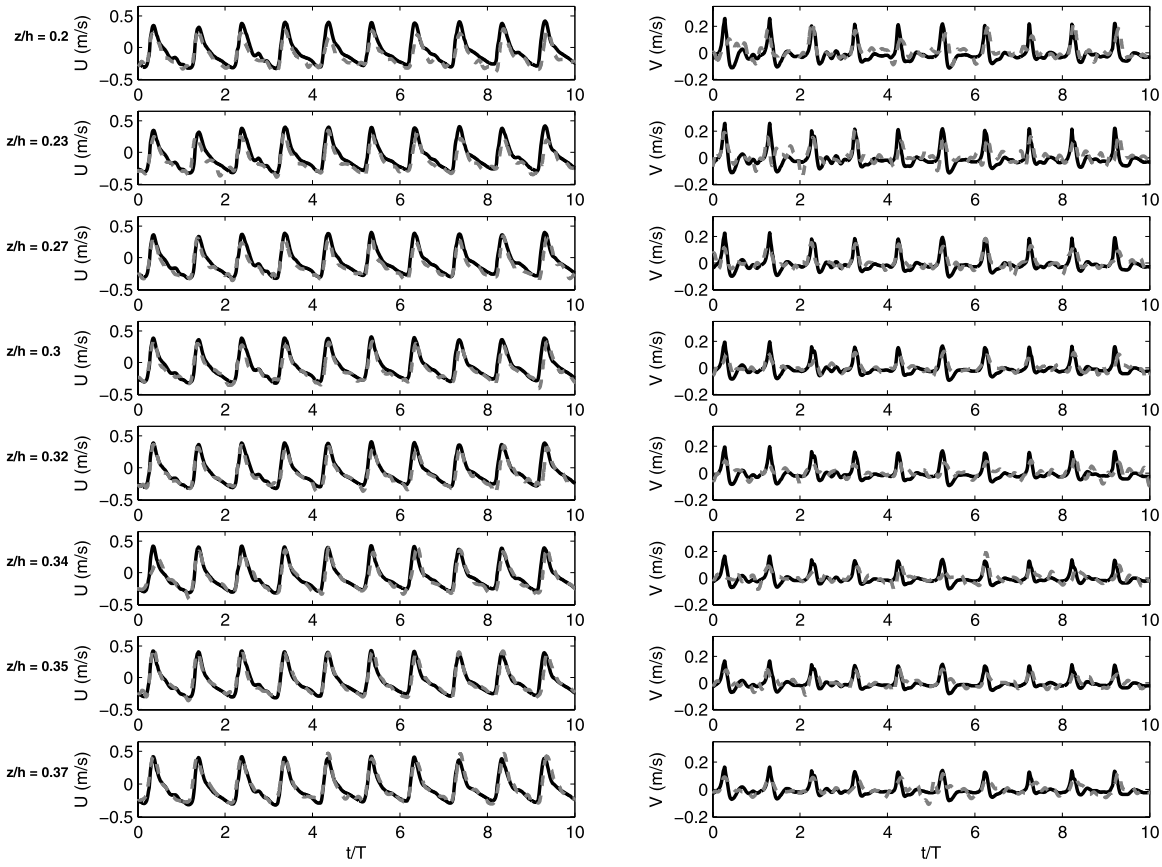

Figure 20. Comparisons between numerical results (solid line) and laboratory experiments (dashed line) of horizontal and vertical velocity time history for case F (H = 0.15 m, T = 2 s) and for a D_{50} = 19 mm gravel size slope at $(x - x_b)/h_b$ = 3.34.

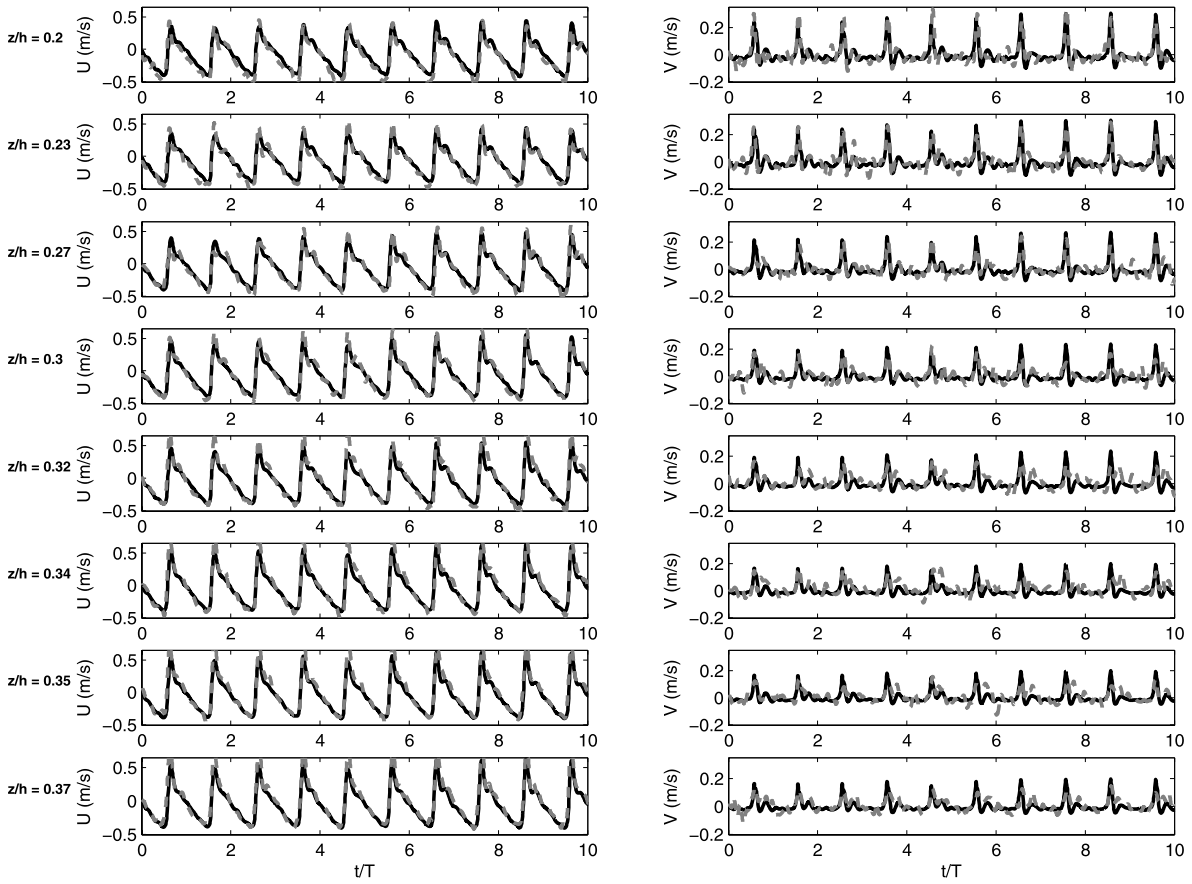

Figure 21. Comparisons between numerical results (solid line) and laboratory experiments (dashed line) of horizontal and vertical velocity time history for case I ($H = 0.15$ m, $T = 3$ s) and for a $D_{50} = 19$ mm gravel size slope at $(x - x_b)/h_b = 6$.

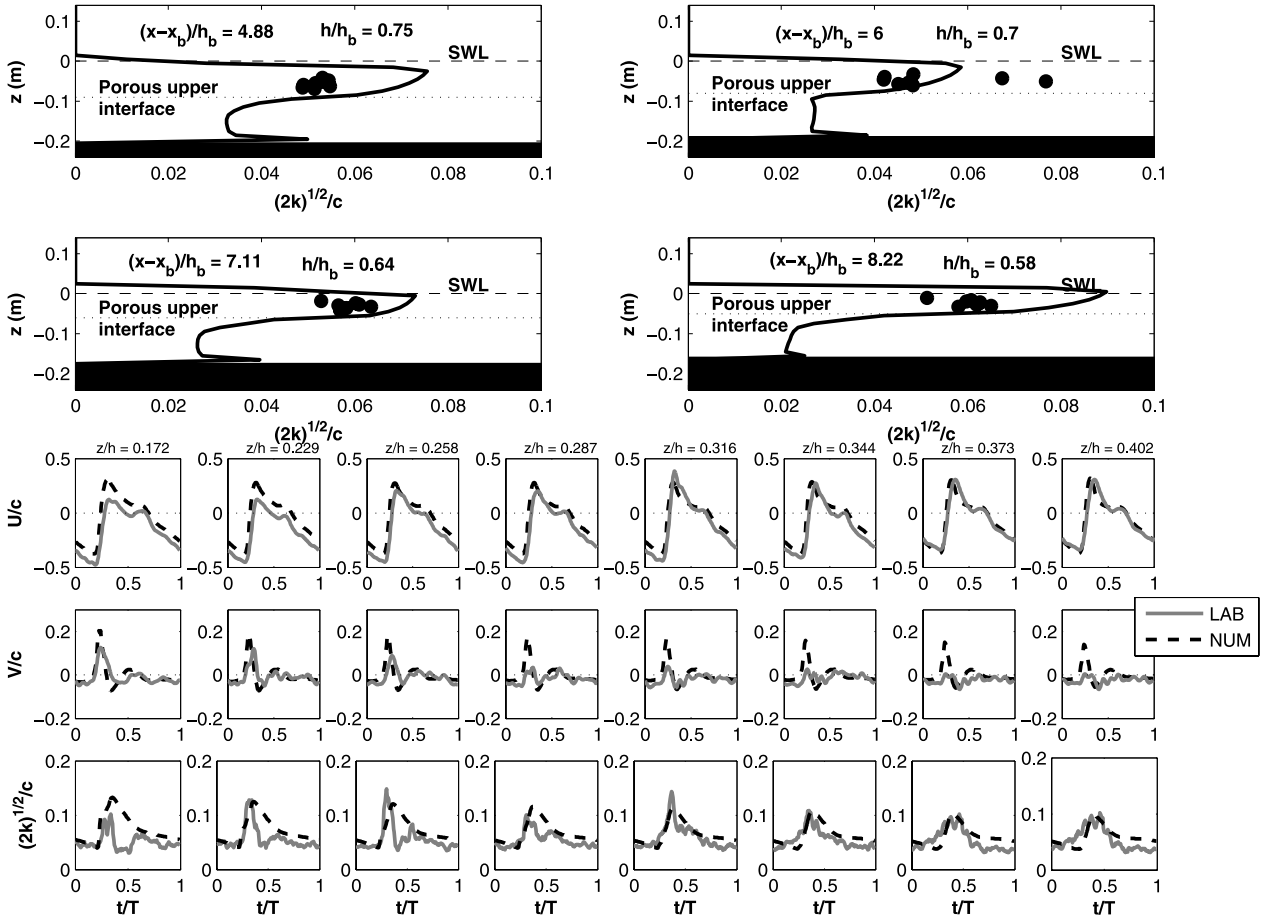

Figure 22. (top four plots) Comparisons between numerical results (solid line) and laboratory experiments (dots) for dimensionless time-mean turbulent intensity for case I (H = 0.15 m, T = 3 s) and for a D_{50} = 19 mm gravel for different locations. (bottom plots) Comparisons of phase averaged magnitudes for normalized horizontal velocity (top row), normalized vertical velocity (middle row), and normalized turbulent intensity (bottom row) at $(x - x_b)/h_b$ = 7.11 for case I (H = 0.15 m, T = 3 s) for a D_{50} = 19 mm gravel size bed.

velocities for different breaking type and bottom characteristics. As in the time-history comparisons large discrepancies are observed close to the bottom. The time-mean TKE is over predicted by the numerical model. Turbulence comparisons are closer for the smaller gravel bed, because of the weaker influence of the bottom. The decreasing with depth vertical distribution of the TKE in the surf zone is simulated by the model. Phase-averaged comparisons for TKE show a better agreement for the wave trough phases than for the wave crest phases that are overpredicted by the model.

[70] Results shown here have proven the capability of a numerical model to go beyond the existing models in simulated wave breaking on a gravel slope. The low number of assumptions and the calibration coefficients used, and the way that the model takes into account the turbulence generation/dissipation mechanisms inside the porous media used show its potential for further applications.

[71] **Acknowledgments.** The authors gratefully acknowledge financial support provided by the Spanish Ministry of Science and Technology under the contract REN2003-09640. They would also like to thank the Fluids Dynamics and Hydraulics Program and the Physical Oceanography Program of the National Science Foundation, Office of Naval Research (Geoscience program) and the National Sea Grant Program through grants to Cornell University.

References

Bonmarin, P. (1989), Geometric properties of deep-water breaking waves, *J. Fluid Mech.*, *209*, 405–433.

Bradford, S. F. (2000), Numerical simulation of surf zone dynamics, *J. Waterw. Port Coastal Ocean Eng.*, *126*, 1–13.

Burcharth, H. F., and O. K. Andersen (1995), On the one-dimensional steady and unsteady porous flow equations, *Coastal Eng.*, *24*, 233–257.

Christensen, E. D. (2006), Large eddy simulation of spilling and plunging breakers, *Coastal Eng.*, *53*, 464–485.

Christensen, E. D., and R. Deigaard (2001), Large eddy simulation of breaking waves, *Coastal Eng.*, *42*, 53–86.

Cox, D. T., and N. Kobayashi (2000), Identification of intense, intermittent coherent motions under shoaling and breaking waves, *J. Geophys. Res.*, *105*, 14,223–14,236.

Garcia, N., J. L. Lara, and I. J. Losada (2004), 2-D numerical analysis of near-field flow at low-crested permeable breakwaters, *Coastal Eng.*, *52*, 43–62.

Hansen, J. B., and I. A. Svendsen (1984), A theoretical and experimental study of undertow, in *Proceedings of the 19th International Conference on Coastal Engineering*, vol. 3, pp. 2246–2262, Am. Soc. of Civ. Eng., Reston, Va.

Harlow, F., and J. Welch (1965), Numerical calculations of time-dependent viscous incompressible flow of fluid with free surface, *Phys. Fluids*, *8*, 2182–2189.

Hirt, C. W., and B. D. Nichols (1981), Volume of fluid (VOF) method for the dynamics of free boundaries, *J. Comput. Phys.*, *39*, 201–225.

Hsu, T.-J., T. Sakakiyama, and P. L.-F. Liu (2002), A numerical model for wave motions and turbulence flows in front of a composite breakwater, *Coastal Eng.*, *46*, 25–50.

Iwata, K., K. Kawasaki, and D. S. Kim (1996), Breaking limit, breaking and post-breaking wave deformation due to submerged structures, in *Proceedings of the 25th International Conference on Coastal Engineering*, vol. 2, pp. 2338–2351, Am. Soc. of Civ. Eng., Reston, Va.

Karambas, T. V. (2003), Modelling of infiltration-exfiltration effects of cross-shore sediment transport in the swash zone, *Coastal Eng. J.*, *45*, 63–82.

Kirby, T. J. (2003), Boussinesq models and applications to nearshore wave propagation, surfzone processes and wave-induced currents, in *Advances in Coastal Engineering*, edited by V. C. Lakhan, pp. 1–41, Elsevier, New York.

Lara, J. L., E. A. Cowen, and I. M. Sou (2002), A depth-of-field limited particle image velocimetry technique applied to oscillatory boundary layer flow over a porous bed, *Exp. Fluids*, *33*, 47–53.

Lara, J. L., N. Garcia, and I. J. Losada (2006), RANS modelling applied to random wave interaction with submerged permeable structures, *Coastal Eng.*, *53*, 395–417.

Lemos, C. M. (1992), A simple numerical technique for turbulent flows with free surfaces, *Int. J. Numer. Methods Fluids*, *15*, 127–146.

Li, T. Q., P. Troch, de J. Rouck, and D. Goossens (2005), Numerical simulation of water wave impacts using a Navier-Stokes solve, in *Proceedings of the 29th International Conference on Coastal Engineering*, pp. 4100–4112, World Sci., Hackensack, N. J.

Lin, P., and P. L.-F. Liu (1998a), A numerical study of breaking waves in the surf zone, *J. Fluid Mech.*, *359*, 239–264.

Lin, P., and P. L.-F. Liu (1998b), Turbulence transport, vorticity dynamics, and solute mixing under plunging breaking waves in surf zone, *J. Geophys. Res.*, *103*, 15,677–15,694.

Lin, P., and P. L.-F. Liu (1999), Internal wave-maker for Navier-Stokes equations models, *J. Waterw. Port Coastal Ocean Eng.*, *125*, 207–217.

Liu, P. L.-F., T.-R. Wu, F. Raichlen, C. E. Synolakis, and J. C. Borrero (2005), Runup and rundown generated by three-dimensional sliding masses, *J. Fluid Mech.*, *536*, 107–144, doi:10.1017/S0022112005004799.

Longo, S., M. Petti, and I. J. Losada (2002), Turbulence in the surf and swash zones: A review, *Coastal Eng.*, *45*, 129–147.

Losada, I. J., J. L. Lara, and N. Garcia (2003), 2-D experimental and numerical analysis of wave interaction with low-crested breakwaters including breaking and flow recirculation, in *Proceedings of Coastal Structures '03*, pp. 863–875, Am. Soc. of Civ. Eng., Reston, Va.

Losada, I. J., J. L. Lara, E. Damgaard, and N. García (2005), Modeling of velocity and turbulence fields around and within low-crested rubble-mound breakwaters, *Coastal Eng.*, *52*, 887–913.

Mendez, F. J., I. J. Losada, and M. A. Losada (2001), Mean magnitudes induced by regular waves in permeable submerged breakwaters, *J. Waterw. Port Coastal Ocean Eng.*, *127*, 7–15.

Mizuguchi, M. (1986), Experimental study on kinematics and dynamics of wave breaking, in *Proceedings of the 20th International Conference on Coastal Engineering*, vol. 1, pp. 589–603, Am. Soc. of Civ. Eng., Reston, Va.

Nadaoka, K., M. Hino, and Y. Koyano (1989), Structure of the turbulent flow field under breaking waves in the surf zone, *J. Fluid Mech.*, *204*, 359–387.

Pedersen, C., R. Deigaard, and J. Sutherland (1993), Turbulent measurements under breaking waves, *Prog. Rep. ISVA 74*, pp. 91–97, Tech. Univ. of Denmark, Lyngby, Denmark.

Peregrine, D. H., and L. A. Svendsen (1978), Spilling breakers, bores and hydraulic jumps, in *Proceedings of the 16th International Conference on Coastal Engineering*, vol. 1, pp. 540–550, Am. Soc. of Civ. Eng., Reston, Va.

Petti, M., and S. Longo (2001), Turbulence experiments in the swash zone, *Coastal Eng.*, *43*, 1–24.

Sakakiyama, T., and P. L.-F. Liu (2001), Laboratory experiments for wave motions and turbulence flows in front of a break water, *Coastal Eng.*, *44*, 117–139.

Shih, R. W. K. (1990), Permeability characteristics of rubble material—New formulae, in *Proceedings of the 22nd International Conference on Coastal Engineering*, vol. 2, pp. 1499–1512, Am. Soc. of Civ. Eng., Reston, Va.

Stive, M. J. F. (1980), Velocity and pressure field of spilling breakers, in *Proceedings of the 17th International Conference on Coastal Engineering*, vol. 1, pp. 547–566, Am. Soc. of Civ. Eng., Reston, Va.

Stive, M. J. F., and H. G. Wind (1982), A study of radiation stress and set-up in the nearshore region, *Coastal Eng.*, *6*, 1–25.

Svendsen, I. A. (1987), Analysis of surf zone turbulence, *J. Geophys. Res.*, *92*, 5115–5124.

Tennekes, H., and J. L. Lumley (1972), *A First Course in Turbulence*, MIT Press, Cambridge, Mass.

Ting, F. C. K., and J. T. Kirby (1994), Observations of undertow and turbulence in a laboratory surf zone, *Coastal Eng.*, *24*, 51–80.

Ting, F. C. K., and J. T. Kirby (1995), Dynamics of surf zone turbulence in a strong plunging breaker, *Coastal Eng.*, *24*, 177–204.

Ting, F. C. K., and J. T. Kirby (1996), Dynamics of surf zone turbulence in a spilling breaker, *Coastal Eng.*, *27*, 131–160.

Troch, P., and J. de Rouck (1998), Development of two-dimensional numerical wave flume for waves interaction with rubble mound breakwaters, in *Proceedings of the 26th International Conference on Coastal Engineering*, vol. 2, pp. 1638–1649, Am. Soc. of Civ. Eng., Reston, Va.

Turner, I. L., and G. Masselink (1998), Swash infiltration-exfiltration and sediment transport, *J. Geophys. Res.*, *103*, 30,813–30,824.

van Gent, M. R. A. (1995), Wave interaction with permeable coastal structures, Ph.D. dissertation, 176 pp., Technical Univ. of Delft, Netherlands.

van Gent, M. R. A., P. Tonjes, H. A. H. Petit, and P. van den Boshe (1994), Wave action on and in permeable structures, in *Proceedings of the 24th International Conference on Coastal Engineering*, vol. 2, pp. 1739–1753, Am. Soc. of Civ. Eng., Reston, Va.

Watanabe, Y., and H. Saeki (1999), Three-dimensional large eddy simulation of breaking waves, *Coastal Eng. J.*, *41*, 281–301.

J. L. Lara and I. J. Losada, Coastal & Ocean Research Group, Escuela Técnica Superior de Ingenieros de Caminos, Canales y Puertos, Universidad de Cantabria, Av. Castros s/n., E-39005 Santander, Spain. (lopezjav@ unican.es; losadai@unican.es)

P. L.-F. Liu, School of Civil and Environmental Engineering, Cornell University, Ithaca, NY 14853, USA. (pll3@cornell.edu)